DRAFT VERSION MAY 2, 2017
Preprint typeset using LaTeX style emulateapj v. 12/16/11

SLAC-PUB-16972

CHARACTERIZING THE POPULATION OF PULSARS IN THE GALACTIC BULGE WITH THE *FERMI* LARGE AREA TELESCOPE.

M. Ajello[1], L. Baldini[2], J. Ballet[3], G. Barbiellini[4,5], D. Bastieri[6,7], R. Bellazzini[8], E. Bissaldi[9,10], R. D. Blandford[11], E. D. Bloom[11], E. Bottacini[11], J. Bregeon[12], P. Bruel[13], R. Buehler[14], R. A. Cameron[11], R. Caputo[15], M. Caragiulo[9,10], P. A. Caraveo[16], E. Cavazzuti[17], C. Cecchi[18,19], E. Charles[11,20,*], A. Chekhtman[21], G. Chiaro[7], S. Ciprini[22,18], D. Costantin[7], F. Costanza[10], F. D'Ammando[23,24], F. de Palma[10,25], R. Desiante[26,27], S. W. Digel[11], N. Di Lalla[2], M. Di Mauro[11,28,*], L. Di Venere[9,10], C. Favuzzi[9,10], E. C. Ferrara[29], A. Franckowiak[14], Y. Fukazawa[30], S. Funk[31], P. Fusco[9,10], F. Gargano[10], D. Gasparrini[22,18], N. Giglietto[9,10], F. Giordano[9,10], M. Giroletti[23], D. Green[32,29], L. Guillemot[33,34], S. Guiriec[29,35], A. K. Harding[29], D. Horan[13], G. Jóhannesson[36,37], M. Kuss[8], G. La Mura[7], S. Larsson[38,39], L. Latronico[26], J. Li[40], F. Longo[4,5], F. Loparco[9,10], M. N. Lovellette[41], P. Lubrano[18], S. Maldera[26], D. Malyshev[31], L. Marcotulli[1], P. Martin[42], M. N. Mazziotta[10], M. Meyer[43,39], P. F. Michelson[11], N. Mirabal[29,35], T. Mizuno[44], M. E. Monzani[11], A. Morselli[45], I. V. Moskalenko[11], E. Nuss[12], N. Omodei[11], M. Orienti[23], E. Orlando[11], M. Palatiello[4,5], V. S. Paliya[1], D. Paneque[46], J. S. Perkins[29], M. Persic[4,47], M. Pesce-Rollins[8], F. Piron[12], G. Principe[31], S. Rainò[9,10], R. Rando[6,7], M. Razzano[8,48], A. Reimer[49,11], O. Reimer[49,11], P. M. Saz Parkinson[50,51,52], C. Sgrò[8], E. J. Siskind[53], D. A. Smith[54], F. Spada[8], G. Spandre[8], P. Spinelli[9,10], H. Tajima[55,11], J. B. Thayer[11], D. J. Thompson[29], L. Tibaldo[56], D. F. Torres[40,57], E. Troja[29,32], G. Vianello[11], K. Wood[58], M. Wood[11,59,*], G. Zaharijas[60,61]

Draft version May 2, 2017

ABSTRACT

An excess of γ-ray emission from the Galactic Center (GC) region with respect to predictions based on a variety of interstellar emission models and γ-ray source catalogs has been found by many groups using data from the *Fermi* Large Area Telescope (LAT). Several interpretations of this excess have been invoked. In this paper we test the interpretation that the excess is caused by an unresolved population of γ-ray pulsars located in the Galactic bulge. We use cataloged LAT sources to derive criteria that efficiently select pulsars with very small contamination from blazars. We search for point sources in the inner $40^\circ \times 40^\circ$ region of the Galaxy, derive a list of approximately 400 sources, and apply pulsar selection criteria to extract pulsar candidates among our source list. We also derive the efficiency of these selection criteria for γ-ray pulsars as a function of source energy flux and location. We demonstrate that given the observed spatial and flux distribution of pulsar candidates, a model that includes a population with about 2.7 γ-ray pulsars in the Galactic disk (in our $40^\circ \times 40^\circ$ analysis region) for each pulsar in the Galactic bulge is preferred at the level of 7 standard deviations with respect to a disk-only model. The properties of these disk and bulge pulsar populations are consistent with the population of known γ-ray pulsars as well as with the spatial profile and energy spectrum of the GC excess. Finally, we show that the dark matter interpretation of the GC excess is strongly disfavored since a distribution of dark matter is not able to mimic the observed properties of the population of sources detected in our analysis.

[1] Department of Physics and Astronomy, Clemson University, Kinard Lab of Physics, Clemson, SC 29634-0978, USA
[2] Università di Pisa and Istituto Nazionale di Fisica Nucleare, Sezione di Pisa I-56127 Pisa, Italy
[3] Laboratoire AIM, CEA-IRFU/CNRS/Université Paris Diderot, Service d'Astrophysique, CEA Saclay, F-91191 Gif sur Yvette, France
[4] Istituto Nazionale di Fisica Nucleare, Sezione di Trieste, I-34127 Trieste, Italy
[5] Dipartimento di Fisica, Università di Trieste, I-34127 Trieste, Italy
[6] Istituto Nazionale di Fisica Nucleare, Sezione di Padova, I-35131 Padova, Italy
[7] Dipartimento di Fisica e Astronomia "G. Galilei", Università di Padova, I-35131 Padova, Italy
[8] Istituto Nazionale di Fisica Nucleare, Sezione di Pisa, I-56127 Pisa, Italy
[9] Dipartimento di Fisica "M. Merlin" dell'Università e del Politecnico di Bari, I-70126 Bari, Italy
[10] Istituto Nazionale di Fisica Nucleare, Sezione di Bari, I-70126 Bari, Italy
[11] W. W. Hansen Experimental Physics Laboratory, Kavli Institute for Particle Astrophysics and Cosmology, Department of Physics and SLAC National Accelerator Laboratory, Stanford University, Stanford, CA 94305, USA
[12] Laboratoire Univers et Particules de Montpellier, Université Montpellier, CNRS/IN2P3, F-34095 Montpellier, France
[13] Laboratoire Leprince-Ringuet, École polytechnique, CNRS/IN2P3, F-91128 Palaiseau, France
[14] Deutsches Elektronen Synchrotron DESY, D-15738 Zeuthen, Germany
[15] Center for Research and Exploration in Space Science and Technology (CRESST) and NASA Goddard Space Flight Center, Greenbelt, MD 20771, USA
[16] INAF-Istituto di Astrofisica Spaziale e Fisica Cosmica Milano, via E. Bassini 15, I-20133 Milano, Italy
[17] Italian Space Agency, Via del Politecnico snc, 00133 Roma, Italy
[18] Istituto Nazionale di Fisica Nucleare, Sezione di Perugia, I-06123 Perugia, Italy
[19] Dipartimento di Fisica, Università degli Studi di Perugia, I-06123 Perugia, Italy
[20] email: echarles@slac.stanford.edu
[21] College of Science, George Mason University, Fairfax, VA 22030, resident at Naval Research Laboratory, Washington, DC 20375, USA
[22] ASI Space Science Data Center, Via del Politecnico snc, 00133 Roma, Italy
[23] INAF Istituto di Radioastronomia, I-40129 Bologna, Italy
[24] Dipartimento di Astronomia, Università di Bologna, I-40127 Bologna, Italy
[25] Università Telematica Pegaso, Piazza Trieste e Trento, 48, I-80132 Napoli, Italy
[26] Istituto Nazionale di Fisica Nucleare, Sezione di Torino, I-10125 Torino, Italy
[27] Università di Udine, I-33100 Udine, Italy
[28] email: mdimauro@slac.stanford.edu
[29] NASA Goddard Space Flight Center, Greenbelt, MD 20771, USA
[30] Department of Physical Sciences, Hiroshima University, Higashi-

This material is based upon work supported by the U.S. Department of Energy, Office of Science, Office of High Energy Physics, under Contract DE-AC02-76SF00515.

1. INTRODUCTION

The Large Area Telescope (LAT) on board the *Fermi* Gamma-ray Space Telescope has been operating since 2008. It has produced the most detailed and precise maps of the γ-ray sky and collected more than 200 million extraterrestrial γ rays in the energy range 0.05–2000 GeV.

The region toward the Galactic Center (GC) is the brightest direction in LAT maps; γ rays from this line of sight (l.o.s.) primarily originate in diffuse processes: interactions of primary cosmic-ray (CR) nuclei with the interstellar gas, bremsstrahlung scattering of CR electrons and positrons with interstellar gas, and inverse Compton scattering of photons from interstellar radiation fields. The LAT also detects individual sources such as pulsars, compact binary systems, supernova remnants, and blazars. In the last seven years many groups analyzing LAT data have reported the detection of an excess of γ-ray emission at GeV energies with an extent of about 20° from the GC (we will refer to this as the GC excess).

The GC excess is found with respect to predictions based on a variety of interstellar emission models (IEMs), point source catalogs, and selections of LAT data (e.g., Goodenough & Hooper 2009; Abazajian & Kaplinghat 2012; Hooper & Slatyer 2013; Gordon & Macías 2013; Abazajian et al. 2014; Calore et al. 2015b; Daylan et al. 2016). This excess is well modeled with a spherically symmetric generalized Navarro-Frenk-White (NFW) (Navarro et al. 1996; Kravtsov et al. 1998) density profile with index 1.25, and its spectral energy distribution (SED) in the inner 10° from the GC is peaked at a few GeV with an intensity that is approximately one tenth of the total γ-ray intensity.

The *Fermi*-LAT Collaboration has performed an analysis using 5.2 years of the Pass 7 reprocessed data in the energy range 1 to 100 GeV for the $15^\circ \times 15^\circ$ region around the GC. This analysis constructed four dedicated IEMs and produced a point-source catalog (designated 1FIG) which includes 48 sources detected in each of the four IEMs with a Test Statistic (TS) larger than 25 [1] (Ajello et al. 2016).

Recently, the *Fermi*-LAT Collaboration published an updated analysis (Ackermann et al. 2017) using data from 6.5 years of observation and the new Pass 8 event-level analysis (Atwood et al. 2013). The Pass 8 event-level analysis significantly improves the acceptance, direction and energy reconstruction, and enables sub-selection of events based on the quality of the direction reconstruction. In this updated analysis further investigations of the systematic uncertainties of modeling the diffuse emission region were made using a variety of templates for additional diffuse γ-ray emission components, such as a data-motivated template for the *Fermi* bubbles (Su et al. 2010; Ackermann et al. 2014), and with an additional population of electrons used in modeling the central molecular zone, and with three different point source lists.

These two analyses confirm the existence the GC excess. However, the energy spectrum of the excess is found to depend significantly on the choice of IEM and source list (Ajello et al. 2016; Ackermann et al. 2017).

Different interpretations have been proposed to explain the GC excess. Its approximately spherical morphology and energy spectrum are compatible with γ rays emitted from a Galactic halo of dark matter (DM). This possibility has been studied in many papers (e.g., Goodenough & Hooper 2009; Abazajian et al. 2014; Calore et al. 2015b; Daylan et al. 2016) and the intensity and shape of the GC excess has been found to be compatible with DM particles with mass 40–60 GeV annihilating through the $b\bar{b}$ channel with a thermally averaged cross section close to the canonical prediction for thermal relic DM (roughly $3 \times 10^{-26}\mathrm{cm}^3\mathrm{s}^{-1}$, e.g., Steigman et al. 2012).

However, if DM exists and gives rise to this excess the same particles should also produce measurable emission from dwarf spheroidal satellite galaxies of the Milky Way, which

[1] The TS is defined as twice the difference in maximum log-likelihood between the null hypothesis (i.e., no source present) and the test hypothesis: $TS = 2(\log \mathcal{L}_{\rm test} - \log \mathcal{L}_{\rm null})$ (see, e.g., Mattox et al. 1996).

Hiroshima, Hiroshima 739-8526, Japan
[31] Erlangen Centre for Astroparticle Physics, D-91058 Erlangen, Germany
[32] Department of Physics and Department of Astronomy, University of Maryland, College Park, MD 20742, USA
[33] Laboratoire de Physique et Chimie de l'Environnement et de l'Espace – Université d'Orléans / CNRS, F-45071 Orléans Cedex 02, France
[34] Station de radioastronomie de Nançay, Observatoire de Paris, CNRS/INSU, F-18330 Nançay, France
[35] NASA Postdoctoral Program Fellow, USA
[36] Science Institute, University of Iceland, IS-107 Reykjavik, Iceland
[37] Nordita, Roslagstullsbacken 23, 106 91 Stockholm, Sweden
[38] Department of Physics, KTH Royal Institute of Technology, AlbaNova, SE-106 91 Stockholm, Sweden
[39] The Oskar Klein Centre for Cosmoparticle Physics, AlbaNova, SE-106 91 Stockholm, Sweden
[40] Institute of Space Sciences (IEEC-CSIC), Campus UAB, Carrer de Magrans s/n, E-08193 Barcelona, Spain
[41] Space Science Division, Naval Research Laboratory, Washington, DC 20375-5352, USA
[42] CNRS, IRAP, F-31028 Toulouse cedex 4, France
[43] Department of Physics, Stockholm University, AlbaNova, SE-106 91 Stockholm, Sweden
[44] Hiroshima Astrophysical Science Center, Hiroshima University, Higashi-Hiroshima, Hiroshima 739-8526, Japan
[45] Istituto Nazionale di Fisica Nucleare, Sezione di Roma "Tor Vergata", I-00133 Roma, Italy
[46] Max-Planck-Institut für Physik, D-80805 München, Germany
[47] Osservatorio Astronomico di Trieste, Istituto Nazionale di Astrofisica, I-34143 Trieste, Italy
[48] Funded by contract FIRB-2012-RBFR12PM1F from the Italian Ministry of Education, University and Research (MIUR)
[49] Institut für Astro- und Teilchenphysik and Institut für Theoretische Physik, Leopold-Franzens-Universität Innsbruck, A-6020 Innsbruck, Austria
[50] Santa Cruz Institute for Particle Physics, Department of Physics and Department of Astronomy and Astrophysics, University of California at Santa Cruz, Santa Cruz, CA 95064, USA
[51] Department of Physics, The University of Hong Kong, Pokfulam Road, Hong Kong, China
[52] Laboratory for Space Research, The University of Hong Kong, Hong Kong, China
[53] NYCB Real-Time Computing Inc., Lattingtown, NY 11560-1025, USA
[54] Centre d'Études Nucléaires de Bordeaux Gradignan, IN2P3/CNRS, Université Bordeaux 1, BP120, F-33175 Gradignan Cedex, France
[55] Solar-Terrestrial Environment Laboratory, Nagoya University, Nagoya 464-8601, Japan
[56] Max-Planck-Institut für Kernphysik, D-69029 Heidelberg, Germany
[57] Institució Catalana de Recerca i Estudis Avançats (ICREA), E-08010 Barcelona, Spain
[58] Praxis Inc., Alexandria, VA 22303, resident at Naval Research Laboratory, Washington, DC 20375, USA
[59] email: mdwood@slac.stanford.edu
[60] Istituto Nazionale di Fisica Nucleare, Sezione di Trieste, and Università di Trieste, I-34127 Trieste, Italy
[61] Laboratory for Astroparticle Physics, University of Nova Gorica, Vipavska 13, SI-5000 Nova Gorica, Slovenia
[*] Corresponding authors: M. Di Mauro, mdimauro@slac.stanford.edu; E. Charles, echarles@slac.stanford.edu; M. Wood, mdwood@slac.stanford.edu.

are known to be DM dominated. No evidence of such a flux from dwarf galaxies has been detected so far, and the limits obtained for the annihilation cross section are in tension with the DM interpretation of the GC excess (see Albert et al. 2017, and references therein).

Among alternative interpretations proposed are that the GeV excess is generated by recent outbursts of CR protons interacting with gas via neutral pion production (Carlson & Profumo 2014) or of CR leptons inverse Compton scattering interstellar radiation (Petrović et al. 2014; Cholis et al. 2015a; Gaggero et al. 2015). However, the hadronic scenario predicts a γ-ray signal that is significantly extended along the Galactic plane and correlated with the distribution of gas, which is highly incompatible with the observed characteristics of the excess (Petrović et al. 2014). The leptonic outburst scenario plausibly leads to a signal that is more smoothly distributed and spherically symmetric; however, it requires at least two outbursts to explain the morphology and the intensity of the excess with the older outbursts injecting more-energetic electrons. An additional population of supernova remnants near the GC that steadily injects CRs is also a viable interpretation for the GC excess (Gaggero et al. 2015; Carlson et al. 2016).

Several authors have examined the properties of detected γ-ray pulsars (PSRs) and found that the unresolved pulsars in the Galactic bulge could account for a significant fraction of the GC excess (Mirabal 2013; Grégoire & Knödlseder 2013; Yuan & Zhang 2014; Petrović et al. 2015; Brandt & Kocsis 2015). Throughout this paper we will use "PSR" to refer specifically to detectable γ-ray pulsars; i.e., pulsars that emit γ-rays and whose γ-ray beams cross the Earth. Typically these have spin-down luminosities above the observed "deathline" of $\sim 3\times10^{33}\,\mathrm{erg\,s^{-1}}$ (Guillemot et al. 2016). The SEDs of PSRs are compatible with the GC excess spectrum and $\mathcal{O}(1000)$ are required to explain its intensity (Hooper & Goodenough 2011; Abazajian 2011; Calore et al. 2014; Cholis et al. 2015b). This Galactic bulge pulsar population is hypothesized to be distinct from the well-known "disk" population that follows the Galactic spiral arms and from which we detect the mostly local known sample of pulsars in radio and γ rays (Manchester et al. 2005; Abdo et al. 2013). See, in particular, Figure 2 of Calore et al. (2016) for an illustration of the Galactic disk and bulge pulsar populations. Finally, since this PSR population would be distributed in the Galactic bulge its spatial morphology could be consistent with that of the GC excess.

This interpretation has been investigated, by, e.g., Cholis et al. (2015b) who claim that about 60 Galactic bulge pulsars should have been already present in *Fermi*-LAT catalogs, though they may not yet be firmly identified as PSRs.

Recently, evidence of the existence of an unresolved population of γ-ray sources in the inner 20° of the Galaxy with a total flux and spatial distribution consistent with the GC excess has been published by Lee et al. (2015) and Bartels et al. (2016). These faint sources have been interpreted as belonging to the Galactic bulge PSR population.

The large amount of data collected by the LAT after 7.5 years of operation and the improvement in energy and spatial resolution brought by Pass 8 enable a deeper search for PSRs in the Galactic bulge. Such a search is highly relevant to testing the potential PSR nature of the GC excess.

Prospects for detecting radio pulsations from the bulge pulsar population were studied by Calore et al. (2016), and the authors found that existing radio pulsar surveys using the Parkes (Keith et al. 2010) and Green Bank (Stovall et al. 2013) telescopes are not quite sensitive enough to detect many pulsars from the bulge population. On the other hand, large area surveys using, e.g., MeerKAT and later SKA (Kramer & Stappers 2015) should detect dozens to hundreds of pulsars from the Galactic bulge.

In this paper we investigate the pulsar interpretation of the GC excess. In Section 2 we present the data selection and the background models that we use. In Section 3 we describe our analysis pipeline and derive a list of sources in the GC region. In Section 4 we study the SEDs of blazars and PSRs detected by the LAT and introduce a criterion to select PSR candidates from our list of sources. In Section 5 we study the distribution of luminosities of known γ-ray PSRs. In Sections 6.1 and 6.2 we model populations of PSRs in the Galactic disk and bulge. In Section 7 we quantify the efficiency of our selection for detecting PSR candidates as a function of direction and flux. In Section 8 we employ a maximum likelihood analysis to derive the characteristics of the Galactic disk and bulge PSR populations. In Section 9 we test whether a smooth distribution of DM could produce the observed distribution of PSR candidates. We summarize our results in Section 10. Details of the data analysis pipeline are provided in the appendices.

2. DATA SELECTION AND BACKGROUND MODELS

The analysis presented in this paper uses 7.5 years of *Fermi*-LAT data recorded between 2008 August 4 and 2016 February 4 (*Fermi* mission elapsed time 239557418–476239414 s). We apply the standard data-quality selections[2].

Since we are interested in detecting the emission from point sources, we select events belonging to the "Pass 8 Source" event class and use the corresponding `P8R2_SOURCE_V6` instrument response functions. In order to minimize the contamination of γ rays generated by cosmic-ray interactions in the upper atmosphere we select events with a maximum zenith angle of 90°. We use events in the energy range $E = [0.3, 500]$ GeV.

We select data for a region of interest (ROI) that is a square of side 40° centered on the GC $(l, b) = (0^\circ, 0^\circ)$, where l and b are the Galactic longitude and latitude, since the GC excess has an extension of approximately 20°.

We employ two different IEMs to estimate the systematic uncertainties introduced by the choice of IEM. The IEMs are brightest in the Galactic disk where the density of interstellar gas and radiation fields is greatest. Additionally, isotropic emission, mainly due to γ-ray emission from unresolved sources (see, e.g., Di Mauro & Donato 2015) and residual contamination from interactions of charged particles in the LAT misclassified as γ rays, is included in the model (Ackermann et al. 2015).

The first IEM we use is the *gll_iem_v06.fits* template, released with Pass 8 data (Acero et al. 2016). The corresponding isotropic component is the *iso_P8R2_SOURCE_V6_v06.txt* template [3]. These are routinely used for Pass 8 analyses and we refer to this model as the official (Off.) model. The second IEM is the Sample model (Ackermann et al. 2017, Section 2.2), from which we remove the GC excess component and add the *Fermi* Bubbles template at $|b| < 10^\circ$ (Ackermann et al. 2017, Section 5.1.3). We refer to that model as the alternate (Alt.) model.

[2] See `http://fermi.gsfc.nasa.gov/ssc/data/analysis`.
[3] For descriptions of these templates see `http://fermi.gsfc.nasa.gov/ssc/data/access/lat/BackgroundModels.html`.

3. ANALYSIS PIPELINE AND SOURCE LIST

We use the `Fermipy` Python package (version 00-11-00)[5] in conjunction with standard LAT `ScienceTools`[6] (version 10-03-00) to find and characterize point sources for both IEMs.

To break the analysis into manageable portions we subdivide the $40^\circ \times 40^\circ$ ROI into 64 smaller $8^\circ \times 8^\circ$ ROIs with an overlap of 3° between adjacent ROIs. Sources near the edge of an ROI are thus well contained in an adjacent ROI. Considering the entire $40^\circ \times 40^\circ$ ROI would imply several hundred free parameters, making the analysis with the LAT `ScienceTools` prohibitive. In each ROI we bin the data with a pixel size of 0.06° and 8 energy bins per decade. In general we analyze each ROI separately; however, as discussed below, at certain points in the analysis we merge information from the analyses of the different ROIs.

The first step of the analysis is to find sources in each of the 64 ROIs. For each ROI we construct an initial model consisting of the IEM, the isotropic template and sources detected with $TS > 49$ in the *Fermi* LAT Third Source Catalog (3FGL, Acero et al. 2015). This provides a reasonably good initial representation of the γ-ray data in each ROI. The procedure selects 116 3FGL sources that we include in the $40^\circ \times 40^\circ$ ROI. As we will show later in this section we recover the vast majority of the least significant 3FGL sources (i.e., those with TS values ranging from 25 to 49).

We then use `Fermipy` tools to refine the positions and the SED parameters of 3FGL sources for the larger, Pass 8 data set that we use here, as well as to find new sources in each ROI. The details of this procedure are described in Appendix A. Since the ROIs overlap slightly, as part of this procedure we remove duplicate sources found in more than one ROI.

We detect 374 (385) sources with $TS > 25$ when using the Off. (Alt.) IEM model. Combining the list of detected sources with each IEM we detect 469 unique sources of which 290 are found with both models. The positions of these sources are displayed in Figure 1, overlaid on a counts map for the $40^\circ \times 40^\circ$ ROI. By comparison, the 3FGL catalog contains 202 sources in this region and 189 (182) of them are found with our analysis with the Off. (Alt.) IEM. The 1FIG, which covered only the inner $15^\circ \times 15^\circ$, contains 48 sources of which we find 38 (41) when we employ in the analysis the Off. (Alt.) IEM. We define associations with 3FGL and 1FIG sources based on the relative positions and the 95% localization uncertainty regions reported in those catalogs and found in our analysis. Specifically, we require that the angular distances of sources in the 3FGL or 1FIG from matching sources in our analysis be smaller than the sum in quadrature of the 95% containment angles in 3FGL or 1FIG and in our analysis. The 3FGL and 1FIG sources that are not present in our lists either have TS near the detection threshold (i.e., $25 < TS < 36$) or are located within $0\overset{\circ}{.}5$ of the GC.

The GC region is the brightest in the γ-ray sky and developing a model of the interstellar emission in this region is very challenging (see, e.g., Calore et al. 2015b; Ajello et al. 2016; Ackermann et al. 2017). Imperfections of our IEMs could manifest themselves as dense concentrations of sources in regions where the IEMs particularly under-predict the diffuse intensity. To account for this, we employed a source cluster-finding algorithm (described in Appendix B) to identify such regions. We find a total of four clusters of sources with four or more sources within $0\overset{\circ}{.}6$ of at least one other source in the cluster. These clusters are located around the GC, in regions around the W28 and W30 supernova remnants and near 3FGL J1814.1−1734c, which is an unassociated source in the 3FGL catalog. (The 'c' designation means that it was flagged in that catalog as possibly an artifact.) These clusters are shown in Figure 1.

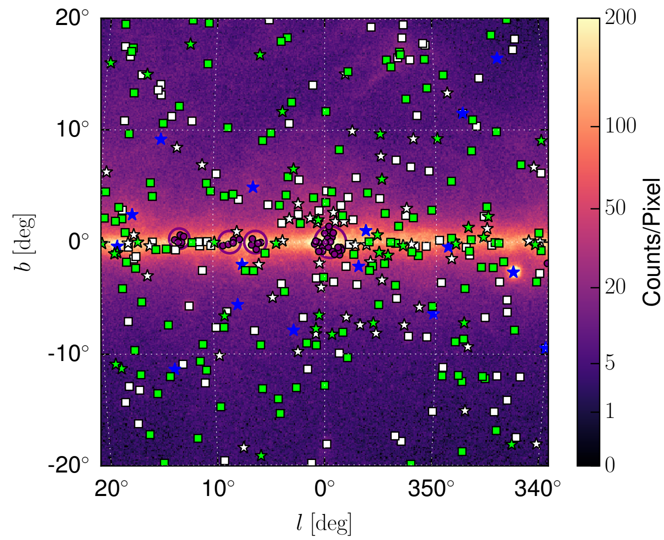

Figure 1. Counts map of the $40^\circ \times 40^\circ$ ROI used in this analysis. The map includes data for the range $[0.3, 500]$ GeV. The map is in Hammer-Aitoff projection, centered on the GC and in Galactic coordinates. The pixel size is 0.1°. The color scale shows the number of photons per pixel. Markers are shown at the positions of sources found in our analysis with the Off. IEM. White markers show sources associated with a 3FGL source and green markers show new sources with no 3FGL counterpart. Stars (squares) indicate sources that are (not) PSR-like and purple markers indicate sources belonging to a cluster, and the clusters are outlined with purple circles (see text for details). Finally, blue stars show PSRs identified as or associated in the 3FGL.

We removed from further consideration here all sources identified as belonging to clusters.

4. SED OF PULSARS AND BLAZARS

In *Fermi*-LAT catalogs, blazars are the most numerous source population. Blazars are classified as BL Lacertae (BL Lacs) or Flat Spectrum Radio Quasars (FSRQs) depending on the presence of strong emission optical lines. In the 3FGL 95% of BL Lac and 85% of FSRQ spectra are modeled with a power-law (PL) function while blazars with a significant spectral curvature (only about 10% of the entire population) are modeled with a log-parabola (LP)[7]. On the other hand, a power law with exponential cutoff (PLE) at a few GeV is the preferred model for pulsars (Abdo et al. 2013). Of the 167 PSRs reported in the 3FGL (143 PSRs identified by pulsations and 24 sources spatially associated with radio pulsars) 115 have spectral fits parametrized with a PLE because they have a significant spectral curvature. The functional definitions of the PL, LP, and PLE spectra are given in Acero et al. (2015).

As described above, spectral shape is a promising observable to separate PSRs from blazars. We fit the spectrum of each source in the ROI and derive the likelihood values for

[5] See `http://fermipy.readthedocs.io/en/latest/`.
[6] See `https://fermi.gsfc.nasa.gov/ssc/`
[7] See `http://fermi.gsfc.nasa.gov/ssc/data/analysis/scitools/source_models.html` for a description of the spectral models implemented in the LAT `ScienceTools`.

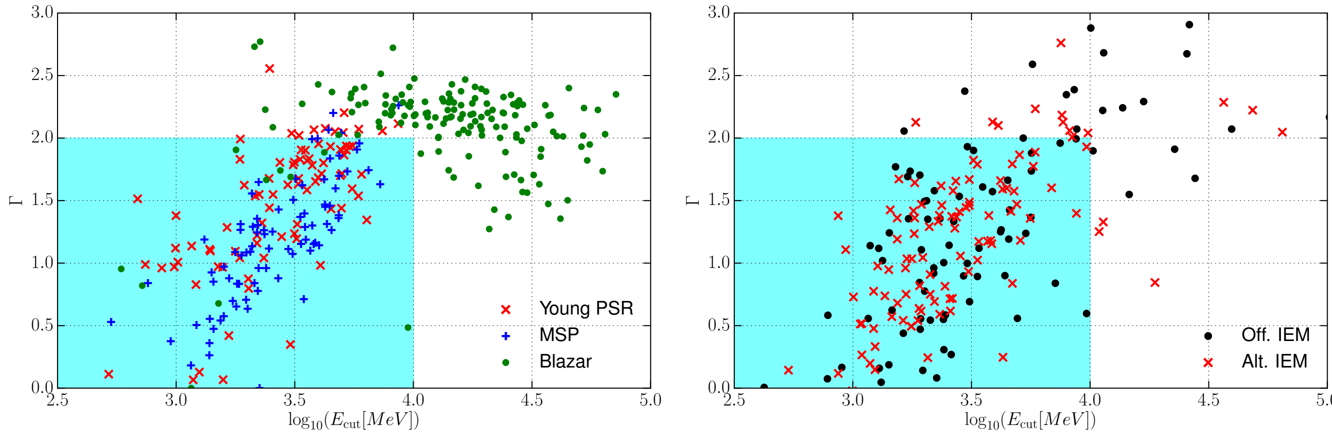

Figure 2. Left: photon index Γ and energy cutoff $E_{\rm cut}$[MeV] of PSRs and blazars detected in our analysis with $TS_{\rm curv}^{\rm PLE} > 9$. MSPs are shown as blue plus signs and young PSRs as red crosses. Here we are showing blazars in the 3FGL (Acero et al. 2015) catalog with curvature significance as in the 3FGL (`Signif_Curve`) larger than 3 (green circles). Right: same as in the left panel but applied to sources in our $40° \times 40°$ ROI detected with $TS_{\rm curv}^{\rm PLE} > 9$ in our analysis with the Off. IEM (black circles) and Alt. IEM (red crosses).

both the PL ($\mathcal{L}_{\rm PL}$) and PLE ($\mathcal{L}_{\rm PLE}$) spectra. We introduce for each source in our analysis the TS for a curved spectrum as: $TS_{\rm curv}^{\rm PLE} = 2 \cdot (\log \mathcal{L}_{\rm PLE} - \log \mathcal{L}_{\rm PL})$. This parameter quantifies the preference to model an SED with a PLE with respect to a PL.

We perform the same analysis on known PSRs and blazars to study the distribution of spectra of these two populations and develop criteria to select PSR candidates. We use the public list of γ-ray PSRs with 210 sources[8] and the subsample of sources identified with or associated with blazars in the 3FGL catalog that have significant spectral curvature. Our blazar sub-sample includes all 3FGL blazars that have `Signif_Curve` greater than 3, where `Signif_Curve` is the significance in standard deviations of the likelihood improvement between PL and LP spectra. We use this subsample to study those blazars most likely to be incorrectly flagged as PSR candidates. This reduced sample of blazars contains 218 objects.

Our definition of $TS_{\rm curv}^{\rm PLE}$ is slightly different from the 3FGL `Signif_Curve` parameter ($\sigma_{\rm curv}$) in that $TS_{\rm curv}^{\rm PLE}$ is defined as the likelihood improvement for a PLE spectrum with respect to the PL spectrum. Furthermore, the 3FGL catalog analysis was based on only 4 years of LAT data. Therefore we used `Fermipy` to re-analyze $10° \times 10°$ ROIs centered around each source in this sample of 210 γ-ray PSRs and 218 blazars. From this re-analysis we derived $TS_{\rm curv}^{\rm PLE}$, the photon index (Γ) and the energy cutoff ($E_{\rm cut}$) for the PLE spectrum.

Of the 210 PSRs, 172 (169) were found to have $TS_{\rm curv}^{\rm PLE} > 9$. The average and standard deviation of their photon indices and energy cutoffs were $\Gamma = 1.33 \pm 0.54 (1.30 \pm 0.54)$ and$\log_{10}(E_{\rm cut}[\rm MeV]) = 3.43 \pm 0.24 (3.40 \pm 0.24)$ when we employed the Off. (Alt.) IEM.

In Table 1 we report the average photon index and cutoff energy for young PSRs (rotational period P greater than 30 ms) and millisecond PSRs (MSPs). The energy cutoff parameter is consistent between young PSRs and MSPs while the average photon index of MSPs is slightly harder.

In the sample of 218 blazars with `Signif_Curve` > 3, 153 have $TS_{\rm curv}^{\rm PLE} > 9$. In the left-hand panel of Figure 2 we show Γ and $\log_{10}(E_{\rm cut})$ for PSRs and blazars detected with $TS_{\rm curv}^{\rm PLE} > 9$. The two populations are well separated in the plotted SED parameters. Taking $\Gamma < 2.0$ and $E_{\rm cut} <$ 10 GeV as selection criteria (shown in cyan in the figure) only 12 blazars, 7% of our blazar sample and less than 1% of the entire 3FGL blazar population, are incorrectly flagged as PSR candidates. Clearly, these selection criteria are effective for distinguishing the PSRs from blazars. Additional studies of the efficiency and false-positive rate of these selection criteria using simulated data are described in Appendix E.

We apply the PSR candidate selection criteria to our source lists. In the list derived with the Off. (Alt.) IEM we find 86 (115) PSR candidates. If we require that the source is selected with both IEMs we find 66 PSR candidates. In the right-hand panel of Figure 2 we show the Γ and $\log_{10}(E_{\rm cut})$ for all sources detected with $TS_{\rm curv}^{\rm PLE} > 9$ for the analysis with the Off. IEM. The average SED parameters for PLE are shown in Table 1. For PSR-like sources detected with both IEMs the photon index (1.02 ± 0.52) is harder with respect to known PSRs (see fifth row in Table 1). This is due to observational biases for the detection of PSRs in direction of the inner part of our Galaxy. We will show this in Section 6.2. We also calculate the integrated energy flux ($S = \int_{E_{\rm min}}^{E_{\rm max}} E dN/dE dE$) over the range from $E_{\rm min} = 300$ MeV to $E_{\rm max} = 500$ GeV.

The full list of sources detected with $TS > 25$ is provided as a FITS file and described in detail in Appendix C. We designate the sources with the prefix '2FIG' designation; however we emphasize that many of the fainter sources in the list are detected only with one of the two IEMs we used.

Globular clusters are gravitationally bound concentrations of ten thousand to one million stars and are the most ancient constituents of our Milky Way Galaxy. They are known to contain many pulsars. Among the detected sources we have 11 globular clusters already identified in the 3FGL and among those, 6 satisfy the PSR-like criteria.

5. LUMINOSITY DISTRIBUTION OF PSRS

Of the 210 identified γ-ray PSRs for which we have good distance estimates, the large majority are located within 4 kpc of the Solar System (see, e.g., Figure 3 of Abdo et al. 2013). They are thus "local" and belong to the Galactic disk population. A pulsar interpretation of the GC excess requires a Galactic bulge population of PSRs. (Throughout this paper

[8] See `https://confluence.slac.stanford.edu/display/GLAMCOG/Public+List+of+LAT-Detected+Gamma-Ray+Pulsars`.

IEM	$N_{\rm PSR}$	Γ	$\log_{10}(E_{\rm cut}[{\rm MeV}])$
Off.	86	1.03 ± 0.52	3.28 ± 0.33
Alt.	115	1.05 ± 0.50	3.27 ± 0.31
Alt. ∩ Off. (Off.)	66	1.02 ± 0.52	3.27 ± 0.32
Alt. ∩ Off. (Alt.)	66	1.01 ± 0.51	3.26 ± 0.30
Known PSRs (Off.)	172	1.33 ± 0.54	3.43 ± 0.24
Young PSRs (Off.)	86	1.46 ± 0.53	3.44 ± 0.26
MSPs(Off.)	86	1.20 ± 0.50	3.42 ± 0.23

Table 1
Spectral parameters of PSR candidates compared with known PSRs.

Note. — Mean values and standard deviations of Γ and $\log_{10}(E_{\rm cut}[{\rm MeV}])$ for PSR candidates compared with known γ-ray PSRs. The first two rows are found using different IEMs (Off. first and Alt. second row). The third (fourth) row is for the PSR candidates detected with both IEMs, computed with the parameters derived in the analysis with the Off. (Alt.) IEM. The last three rows list the parameters for all γ-ray PSRs, young PSRs and MSPs detected with $TS_{\rm curv}^{\rm PLE} > 9$.

we adopt 8.5 kpc as the distance to the GC.) However the known Galactic disk PSR population is a strong foreground to the putative Galactic bulge population. In this section we describe simulations of the Galactic disk and bulge populations that are based on the morphology and energy spectrum of the GC excess and the characteristics of 3FGL PSRs. We then use these simulations to estimate the number of sources in these populations that would be needed to match both the observed GC excess and the numbers and properties of the detected sources in the $40^\circ \times 40^\circ$ ROI.

To perform these simulations (and those described in Section 7), we use `Fermipy` as explained in Appendix D to generate simulated data sets of the individual ROIs and then use the analysis pipeline described in Section 3 to analyze those simulated maps. For these simulations we used the same time and energy ranges and the same ROI as the analysis on the real sky, and we employed the Off. IEM.

For the simulations described in this section we simulate blazars isotropically distributed in the $40^\circ \times 40^\circ$ ROI, with fluxes taken from the dN/dS derived by Abdo et al. (2010b) using the 1FGL catalog (Abdo et al. 2010a). We simulated individual blazars using a PL SED with Γ extracted from a Gaussian distribution with average 2.40 and standard deviation 0.30 as found for the 3FGL (Acero et al. 2015). We simulated blazars with an energy flux integrated between $0.3-500$ GeV of $> 9 \times 10^{-8}$ MeV cm^{-2} s^{-1} in order to have a sizable number of simulated sources below the detection threshold.

To model the Galactic disk and bulge PSR populations, ideally we would start with a known luminosity function for PSRs, or derive one starting with the 210 publicly announced γ-ray PSRs. However, because of complications including the incompleteness of the radio pulsar sample and variations in detection efficiency across the sky, and since the PSR sample covers the entire sky well beyond our ROI, the PSR luminosity function is poorly constrained and difficult to extract. See, e.g., Strong (2007); Cholis et al. (2014); Petrović et al. (2015); Bartels et al. (2016) both for previous estimates of the luminosity function and for discussions of the complications.

Therefore we adopt a staged approach. We first assume a PL shape $dN/dL \propto L^{-\beta}$ for the luminosity function and estimate the slope (β) from the data as described below. We then derive the normalization given that slope by using simulations (Section 6) to estimate the number of γ-ray pulsars that would be required to explain the GC excess and energy flux distribution of 3FGL sources with curved SEDs using simulations. Finally, we reuse those simulations to derive the efficiency for PSRs to pass our selection criteria.

Given for each PSR the energy flux S and distance d we calculate the luminosity: $L = 4\pi S d^2$, where S is integrated in the energy range $0.3-500$ GeV, [9] as derived with the analysis described in Section 4 and the distance (d) is taken from the ATNF catalog version 1.54 (Manchester et al. 2005) using the continuously updated web page [10]. The catalog provides distance measures for 135 out of 210 PSRs and from these we can derive the observed luminosity distribution dN/dL. The missing 75 pulsars are mostly *Fermi* γ-loud and radio-quiet. We also calculate the dN/dL separately for young PSRs and MSPs without correcting for the detection efficiency.

Since the PSR sample detected by the LAT is known to be incomplete and we do not correct for the detection efficiency we select sources within a distance of 3 kpc from the Earth. Indeed, considering luminosities in the range $[3 \times 10^{33}, 10^{36}]$ erg s^{-1} and a distance of 3 kpc implies energy fluxes in the range $[3 \times 10^{-6}, 6 \times 10^{-4}]$ MeV cm^{-2} s^{-1} for which the LAT efficiently detects sources. In Figure 3 we show the luminosity distribution for our sample of PSRs with $d < 3$ kpc. We then perform a fit to the data starting from $L = 3 \times 10^{33}$ erg s^{-1} to avoid the change in slope at low luminosities due to the incompleteness of the LAT detections at the low-luminosity end. We use a PL shape $dN/dL \propto L^{-\beta}$ and the fit yields $\beta = 1.20 \pm 0.08$. Our fit differs from the data points only below $3-5 \times 10^{32}$ erg s^{-1} where it is difficult to identify PSRs with γ-ray data.

Our estimate of β for PSRs with $L_\gamma > 3 \times 10^{33}$ erg s^{-1} is similar to that found for MSPs by Cholis et al. (2014); Hooper & Mohlabeng (2016); Winter et al. (2016). In these papers a break at around 10^{33} erg s^{-1} or a slightly curved luminosity function is considered. However, since the slope of the luminosity function is 1.20, the integrated luminosity is dominated by the bright sources. Therefore, a change of dN/dL below 10^{33} erg s^{-1} does not significantly affect our results. We also point out that Winter et al. (2016) have estimated the completeness of the Second *Fermi*-LAT catalog of pulsars (Abdo et al. 2013) finding that it is almost 100% for pulsars with luminosity greater than 10^{35} erg s^{-1}. The least-luminous PSR detected is $5 \cdot 10^{31}$ erg s^{-1} while the most luminous is 10^{36} erg s^{-1}. We therefore simulate luminosities between 10^{31} erg s^{-1} and 10^{36} erg s^{-1} to include PSRs below the current LAT detection threshold. Furthermore, throughout this paper, we quote the total number of PSRs with $L = [10^{31}, 10^{36}]$ erg s^{-1} in the Galactic disk ($N_{\rm disk}$) and bulge ($N_{\rm bulge}$) to specify the normalization of dN/dL.

6. SIMULATING THE GALACTIC PSR POPULATION

In this section we report our assumptions for the disk and Galactic bulge populations of PSRs and explain how we simulate these two populations.

6.1. *Galactic Disk PSRs*

For our simulations we use the Galactocentric spatial distribution $\rho(R)$ as modeled by Lorimer (2004): $\rho(R) \propto R^n \exp{(-R/\sigma)}$ with $n = 2.35$ and $\sigma = 1.528$ kpc. The dependence on the distance from the Galactic disk is modeled with an exponential cutoff $\rho(z) \propto \exp{(-|z|/z_0)}$ with scale

[9] Note that this differs from previous publications, which use 100 MeV as the lower bound of the integration range for the luminosity.

[10] We always use the *Dist_1* parameter, namely the best distance estimate available, when it exists (see the ATNF catalog for more information: `http://www.atnf.csiro.au/people/pulsar/psrcat/`).

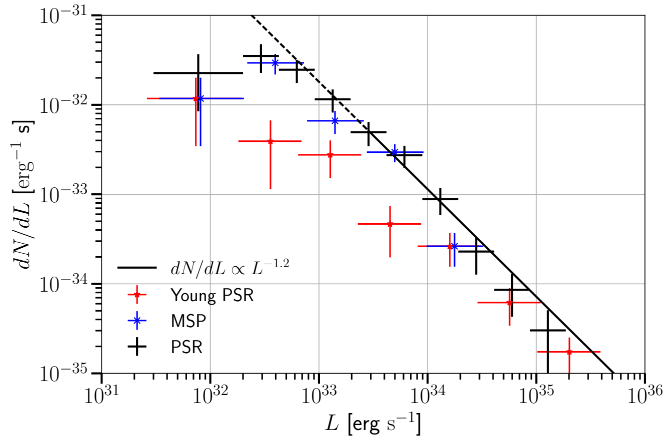

Figure 3. Observed luminosities for young PSRs (red data), MSPs (blue data) and the whole population of PSRs with $d < 3$ kpc (black data). The best fit to the luminosity distribution for $L > 3 \times 10^{33}$ erg s^{-1} is also reported (black line). The luminosity is integrated over the energy range [0.3, 500] GeV.

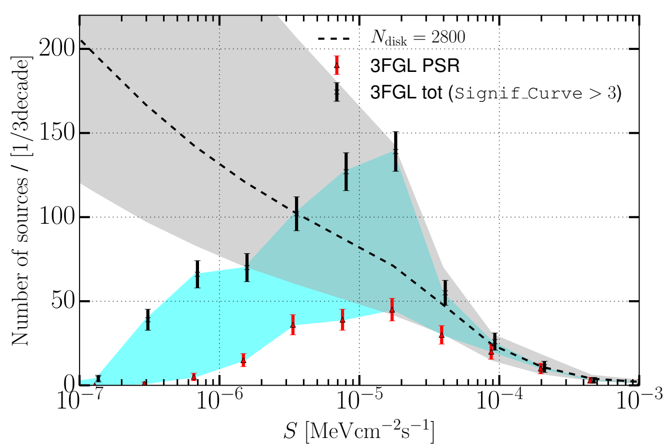

Figure 4. Flux histogram of 3FGL PSRs alone (red triangles) or added to the flux distribution of unassociated 3FGL sources with curvature `Signif_Curve` > 3 (black points). The cyan band represents the region between the lower limit (already detected PSRs) and upper limit (3FGL PSRs plus unassociated 3FGL sources with detected spectral curvature). Finally the black curve (gray band) represents the benchmark (band between the minimum and maximum) number of disk PSRs. The flux is integrated over the energy range [0.3, 500] GeV.

height $z_0 = 0.70$ kpc as in Calore et al. (2014). The luminosity function is modeled as a PL with index 1.20 over the range $L = [10^{31}, 10^{36}]$ erg s^{-1}, see Section 5.

Analyses of the Galactic disk pulsar population estimate that it could contain thousands of objects (Levin et al. 2013; Lorimer 2013, 2004). These estimates are derived from radio catalogs of pulsars, correcting their spatial distribution for observational biases and using information for the star formation rate and distribution in the Galaxy.

However, the radio and the γ-ray emission are only slightly correlated and many of the nearest radio pulsars are not detected by the LAT. The current ATNF catalog lists 714 pulsars within 3 kpc of the Earth that have measured spin down energy loss rates ($\dot{E}$). Of these, 257 have $\dot{E} > 10^{33}$ erg s^{-1}, the observed minimum for which pulsars emit γ rays (Guillemot et al. 2016). The LAT has detected about 30% of these, most likely primarily due to differences in radio and γ-ray emission beam solid angles of the source and to their distances.

In short, the overall number of γ-ray PSRs in the disk population is not very well constrained. A lower limit is given by the identified γ-ray PSRs: in particular, for fluxes integrated between $0.3 - 500$ GeV larger than 10^{-5} MeV cm^{-2} s^{-1} where the efficiency for the detection of PSRs is almost 100% (see Section 7). In Figure 4 we show the energy flux histogram for 3FGL PSRs.

This is, however, only a lower limit because many non-radio PSRs may be present as sources in the 3FGL, but the pulsations have not yet been detected in γ rays. Without timing solutions from radio observations, the detection of γ-ray pulsation is challenging; see e.g., Dormody et al. (2011) for a sensitivity estimate. To obtain an estimate of the upper limit of PSRs in the disk we have selected the 3FGL unassociated sources with curvature significance greater than 3. We added their flux distribution to that of the detected PSRs (Figure 4). We expect that the bright tail ($S > 1.8 \cdot 10^{-5}$ MeV cm^{-2} s^{-1}) of the flux distribution for the disk population of PSRs should fall between the already detected PSRs (111) and the sum of this with 3FGL unassociated sources with $\sigma_{\rm curv} > 3$ (237). This range is represented by the cyan band in Figure 4. From this we estimate that the Galactic disk PSR population consists of between 1400 and 5600 γ-ray emitting sources with $L > 10^{31}$ erg s^{-1}, i.e., $N_{\rm disk} \in [1400, 5600]$. This result is derived with the Galactocentric spatial distribution as modeled by Lorimer (2004) and it slightly depends on the assumed radial distribution of PSRs in the disk. The flux distribution of this disk population is displayed with a gray band in Figure 4 and for energy fluxes larger than 10^{-5} MeV cm^{-2} s^{-1} is perfectly consistent with the cyan band. In Section 8 we will use this constraint on the total number of bright Galactic disk PSRs to constrain the number of Galactic disk PSRs in our $40° \times 40°$ ROI.

6.2. *Galactic Bulge PSRs*

We model the spatial distribution of the Galactic bulge PSR population as spherically symmetric with respect to the GC with a radial profile $dN/dr \propto r^{-\alpha}$ for $r < 3$ kpc and 0 elsewhere and with $\alpha = 2.60$ in order to approximately match a generalized NFW with slope of 1.3. This spatial distribution is consistent with the morphology of the GC excess (Calore et al. 2015b; Daylan et al. 2016; Ajello et al. 2016; Ackermann et al. 2017) and gives a latitude profile of the γ-ray intensity from PSRs with a similar shape to the excess (see left-hand panel Figure 5). As with the disk population, we model the luminosity function as a PL with $\beta = 1.20$ over the range $L = [10^{31}, 10^{36}]$ erg s^{-1}. For each simulated PSR we draw a location and luminosity from the relevant spatial distribution and γ-ray PSR luminosity function and sample values from the distributions of Γ and $\log_{10}(E_{\rm cut})$ given in the fifth row of Table 1. We then derive the SED of each PSR, and simulate PSRs until their total energy spectrum is of the same intensity as the GC excess as reported by Calore et al. (2015b) and Ajello et al. (2016).

In the left panel of Figure 5 we compare the average latitude profile from 20 simulations with the intensity of the GC excess and in the right panel we compare the total SED from simulated PSRs and the GC excess spectrum as derived by Calore et al. (2015b) and Ajello et al. (2016). The gray band in both plots is derived from the possible range of source counts that this component could contain and includes the reported systematic uncertainties of the latitude profile and energy spectrum of the GC excess. This procedure constrains the Galactic bulge PSR population to include 500–2300 sources with $L > 10^{31}$ erg s^{-1}, i.e., $N_{\rm disk} \in$

$[500, 2300]$.

6.3. *Full Model*

Our benchmark model for sources in the $40^\circ \times 40^\circ$ ROI has $N_{\rm bulge} = 1300$ PSRs, $N_{\rm disk} = 2800$ PSRs and about 900 blazars. In Figure 6 we show the positions of the simulated PSRs and blazars for one realization. With this realization of the analysis we detect (with $TS > 25$) 77 (128) PSRs from the Galactic bulge (disk) and 92 blazars.

If we select only objects that satisfy the PSR candidate selection criteria we find 56 (82) PSRs from the Galactic bulge (disk) and 1 blazar, for a total of 138 PSRs with negligible contamination from blazars. The sum of 3FGL PSRs and the PSR candidates found with our analysis of the $40^\circ \times 40^\circ$ ROI is 116 (151) with the Off. (Alt.) IEM, which is consistent with the 138 PSRs found in this simulated realization of the analysis. Finally, the average and standard deviation of the measured photon indices and energy cutoffs of detected PSRs are $\Gamma = 1.10 \pm 0.60$ and $\log_{10}(E_{\rm cut}[{\rm MeV}]) = 3.37 \pm 0.24$. Thus, the measured energy cutoffs are consistent both with what we find for the real sky (see Table 1) and with the simulation input. On the other hand, the photon index distribution is consistent with what we find for the real sky but harder than the simulation input; we attribute the difference to selection bias favoring harder-spectrum PSRs.

7. EFFICIENCY FOR THE DETECTION OF PULSAR CANDIDATES AND SOURCE CONFUSION

In this section we derive the sensitivity of the LAT for detecting PSRs in our $40^\circ \times 40^\circ$ ROI. Specifically, we derive the efficiency, $\omega(l, b, S)$ with which a PSR in a given direction in the Galaxy (l, b) and with a given energy flux, S, is detected as a point source ($TS > 25$) and satisfies our PSR selection criteria: $TS_{\rm curv}^{\rm PLE} > 9$, $E_{\rm cut} < 10$ GeV and $\Gamma < 2.0$.

We use simulated realizations of LAT data sets to measure $\omega(l, b, S)$. These simulations are largely similar to those described in Secs. 5 to 6.2, with some differences in the source distributions, as described below.

We generate 10 simulations of the $40^\circ \times 40^\circ$ ROI with a Galactic bulge population of PSRs (1300 on average) and an isotropic distribution of 2800 PSRs. We use an isotropic distribution of PSRs and 10 simulations in order to have a good coverage of the spatial distribution and energy flux of detected and simulated sources. We simulate only PSRs with `Fermipy` as explained in Appendix D, without considering cataloged sources. We consider the same time and energy range, the same ROI and we employ the Off. IEM. Since the goal is to find the efficiency for the detection of PSR-like sources we do not simulate blazars.

We analyze each simulation using the same pipeline employed for the real data. We bin the sources by Galactic longitude and latitude and the simulated energy flux ($S^{\rm true}$) and we count the number of simulated and detected (with $TS_{\rm curv}^{\rm PLE} > 9$, $E_{\rm cut} < 10$ GeV and $\Gamma < 2.0$) sources in each bin. For a bin centered at (l_i, b_j) and with the geometric mean energy ($S_k^{\rm true}$), the efficiency $\omega(l_i, b_j, S_k^{\rm true})$ is calculated as the ratio of the detected ($N_{i,j,k}^{\rm det}$) and simulated ($N_{i,j,k}^{\rm true}$) PSRs in that bin ($\omega_{i,j,k} \equiv \omega(l_i, b_j, S_k^{\rm true}) = N_{i,j,k}^{\rm det}/N_{i,j,k}^{\rm true}$).

In Figure 7 we show ω as a function of latitude and energy flux. The efficiency ω is very small near the Galactic plane due to the bright foregrounds that make the detection of PSRs more difficult in this region with respect to the outer directions and to complications from source confusion. Considering $|b| > 6^\circ$, ω does not change significantly and it is almost unity for energy fluxes greater than 10^{-5} MeV cm^{-2} s^{-1}, meaning that almost all such sources are detected and pass the PSR selection criteria.

Gamma-ray PSRs within a few degrees of the GC are difficult to detect not only because of the foregrounds but also owing to source confusion. In Figure 8 we show for each detected PSR candidate the number of simulated sources that are within its 95% positional uncertainty. These numbers are averaged over 10 realizations. A source detected with $TS > 25$ within 0.1° of the GC has on average 300 simulated sources within its 95% positional uncertainty. The majority of these simulated sources are too faint to be detected but their total emission gives a significant contribution to the background flux and complicates the source detection.
To study the effects of source confusion we simulate an isotropic distribution of PSRs at $(l, b) = (10^\circ, 10^\circ)$ and in a $10^\circ \times 10^\circ$ region. We generate distributions of PSRs with an increasing number of sources in this region employing source densities in the range 0.1–300 source deg^{-2}. Source densities of 0.65/2.8/14 source deg^{-2} are found at longitudes and latitude $(l, b) = (15^\circ, 15^\circ)/(15^\circ, 0^\circ)/(0^\circ, 0^\circ)$ given a disk population of 2800 PSRs, a bulge population of 1300 PSRs and 900 blazars, with the models explained in the Section 6.

We simulate PSRs with energy fluxes uniformly extracted in the range (2–3)$\times 10^{-6}$ MeV cm^{-2} s^{-1} for which the efficiency is about 50% at latitudes $|b| > 5^\circ$ (see Figure 7). We analyze each simulation and we find for each source density setup the efficiency for the detection of PSR-like sources. We show the results in Figure 9. For source densities lower than 5 deg^{-2} the efficiency is around 0.5 and constant within uncertainties. For larger densities, ω decreases rapidly due to source confusion and more precisely because many bright sources are present in the same region and it becomes increasingly difficult to detect sources individually. We thus have demonstrated that source confusion affects our estimation of the efficiency only when the source density is 5 deg^{-2} and; these densities are reached only in the inner few degrees from the GC, where, in fact, we have found a cluster of sources that we removed from consideration for the rest of our analysis (see Figure 1). Thus, the effects of source confusion have already been incorporated in our evaluation of the efficiency.

As we have previously stated, we simulated an isotropic distribution of PSRs in order to have a good spatial coverage of sources in the entire ROI. Simulating a disk population of 2800 PSRs would have increased the density of sources in the inner few degrees from the GC only by a few percent and would not substantially affect our conclusions on source confusion.

To model the number of PSR candidates detected from the Galactic disk and bulge PSR populations, for any given measured energy flux $S^{\rm obs}$ we need to know the fraction of simulated PSRs that are detected. However the efficiency defined above is a function of the simulated energy flux $S^{\rm true}$. The fractional difference between $S^{\rm true}$ and $S^{\rm obs}$ is significant for sources detected near the sensitivity threshold while it is negligible for very bright sources.

We correct for this with the following formalism. We introduce the corrected efficiency $\Omega_{i,j,k,m} \equiv \Omega(l_i, b_j, S_k^{\rm obs}, S_m^{\rm true})$, which can be derived as:

$$\Omega_{i,j,k,m} = N_{i,j}^{\rm det}(S_k^{\rm obs}|S_m^{\rm true})/N_{i,j}^{\rm model}(S_m^{\rm true}). \qquad (1)$$

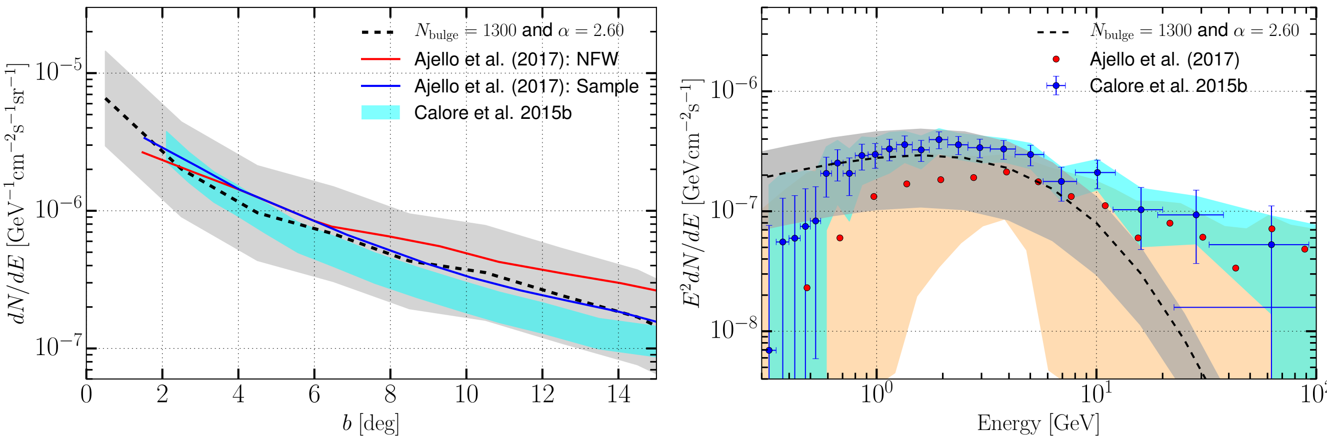

Figure 5. Left panel: latitude profile of the intensity of the GC excess at 2 GeV and longitude 0° for PSRs in the Galactic bulge with $N_{\rm bulge} = [500, 2300]$ (gray band and black dashed line), and for the GC excess as found by Calore et al. (2015b) (cyan band) and Ajello et al. (2016) (blue and red solid curves). Right panel: energy spectrum from all PSRs in the Galactic bulge with $N_{\rm bulge} = [500, 2300]$ (gray band and black dashed line), and for the GC excess as found by Calore et al. (2015b) (cyan band and blue data) and Ajello et al. (2016) (orange band and red data).

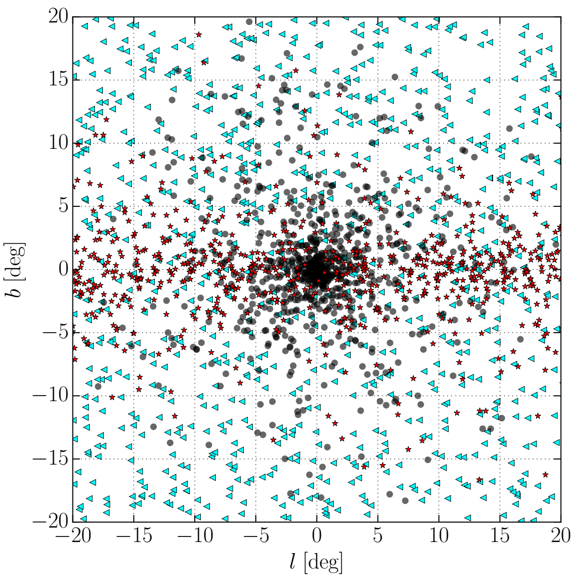

Figure 6. Positions of all simulated blazars (cyan triangles), Galactic disk (red stars) and Galactic bulge (black circles) PSRs from a single realization of the 40° × 40° ROI.

This quantity gives the probability for the measured energy flux to be in energy bin k given a simulated source whose true energy flux is in energy bin m, for the spatial bin i, j. Figure 10 shows Ω averaged over the $40° \times 40°$ ROI and with the energy binning used in the analysis described in Section 8. For a PSR distribution with $N^{\rm model}_{i,j}(S^{\rm true}_m)$ sources in a given spatial bin and true energy flux bin ($S^{\rm true}_m$), the number of PSR candidates for an observed energy flux bin $S^{\rm obs}_k$ is given by:

$$N^{\rm obs}_{i,j,k} = \sum_m \Omega_{i,j,k,m} \cdot N^{\rm model}_{i,j}(S^{\rm true}_m) \qquad (2)$$

We will use this formalism in the next section to characterize the Galactic disk and bulge populations of PSRs.

8. CHARACTERIZING THE GALACTIC DISK AND BULGE PSR POPULATIONS

In the previous sections we described simulating Galactic disk and bulge PSR populations and estimating the number of detected PSR candidates expected from these populations. In this section we employ a maximum likelihood analysis to constrain the properties of these PSR populations.

We define the number density of PSRs per volume element (dV) as a function of position around the GC and luminosity (dL): $dN/(dV dL) = \rho \cdot dN/dL$ where $\rho(r)$ is the density of PSRs, taken from Lorimer (2004) for the Galactic disk PSR population and assumed $\propto r^{-\alpha}$ for the Galactic bulge PSR population. We convert this quantity to the number of PSRs $N_{i,j,k}$ for a particular pixel of solid angle $\Delta\Omega_{i,j}$ and bin of energy flux ΔS using:

$$N^{\rm model}_{i,j,k} = \sum_m \Omega_{i,j,k,m} \int_{\Delta\Omega_{i,j}} dl \cos b db \int_0^\infty ds \rho(r(l,b,s)) s^2 \times \int_{L^{\rm min}_m}^{L^{\rm max}_m} \frac{dN}{dL} dL, \qquad (3)$$

where s is the distance, $L^{\rm min}_m = 4\pi s^2 S^{\rm min}_m$ and $L^{\rm max}_m = 4\pi s^2 S^{\rm max}_m$, $S^{\rm min}_m$ and $S^{\rm max}_m$ are the extremes of the energy flux bin centered on S_m, r is the distance from the GC and $\Delta\Omega_{i,j}$ is the solid angle of the pixel centered on (l_i, b_j).

The number of PSR candidates predicted by our model depends on several parameters: β the slope of the luminosity function (1.20 in our benchmark model), $N_{\rm disk}$ the number of Galactic disk PSRs, z_0 the scale height of the distribution of sources out of the Galactic plane (equal to 0.70 kpc as in Calore et al. (2014)), (n, σ) the parameters of the disk population of PSRs ($n = 2.35$ and $\sigma = 1.528$ as in Lorimer (2004)), $N_{\rm bulge}$ the number of PSRs in the Galactic bulge population and α the slope of the radial profile of this component ($\alpha = 2.6$).

We maximize the log-likelihood $\log(\mathcal{L})$ to estimate the best-fit values of these parameters:

$$\log(\mathcal{L}) = \sum_{i,j,k} N^{\rm obs}_{i,j,k} \log(N^{\rm model}_{i,j,k}(\lambda)) + N^{\rm model}_{i,j,k}(\lambda) + \mathcal{L}_{\rm prior}, \qquad (4)$$

where the first term is the Poisson log-likelihood, λ is the set of parameters that we include in the fit and $\mathcal{L}_{\rm prior}$ is a prior taken from the results presented in Section 6.1 that constrains the number of PSRs using the results of the bright part of the energy flux distribution ($N^{\rm data}_{S>S_0}$, with $S_0 = 1.8 \cdot 10^{-5}$ MeV

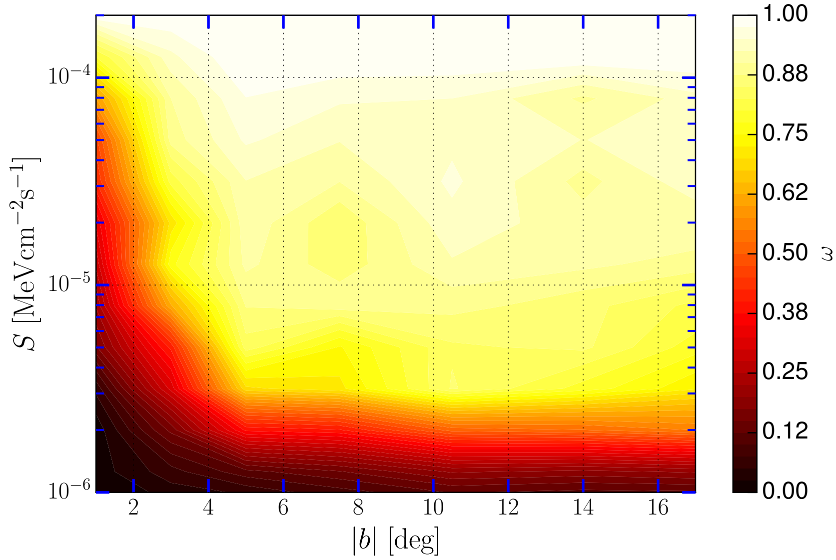

Figure 7. Efficiency ω for the detection of a PSR candidate as a function of latitude $|b|$ and energy flux S This plot is averaged over 20° of longitude around the GC and the flux is integrated over $[0.3, 500]$ GeV and corresponds to 7.5 years of data selected as described in Section 2.

	Alternate IEM						Official IEM					
A	$N_{\rm disk}$	z_0[kpc]	β	$N_{\rm bulge}$	α	TS	$N_{\rm disk}$	z_0[kpc]	β	$N_{\rm bulge}$	α	TS
1	23500^{+5500}_{-5000}	$0.63^{+0.14}_{-0.14}$	$1.35^{+0.07}_{-0.07}$	0	$\cdots$	0	22500^{+5200}_{-4800}	$0.71^{+0.16}_{-0.16}$	$1.34^{+0.07}_{-0.07}$	0	$\cdots$	0
2	3740^{+1030}_{-940}	$0.66^{+0.14}_{-0.14}$	$1.23^{+0.06}_{-0.06}$	1580^{+330}_{-270}	2.60	60	3560^{+980}_{-870}	$0.72^{+0.17}_{-0.17}$	$1.24^{+0.06}_{-0.06}$	1330^{+270}_{-210}	2.60	63
3	3960^{+1070}_{-970}	$0.70^{+0.16}_{-0.16}$	$1.24^{+0.07}_{-0.07}$	1660^{+350}_{-300}	$2.55^{+0.24}_{-0.24}$	65	3610^{+1010}_{-930}	$0.75^{+0.18}_{-0.18}$	$1.25^{+0.07}_{-0.07}$	1370^{+280}_{-220}	$2.57^{+0.23}_{-0.23}$	69
B	$N_{\rm disk}$	z_0[kpc]	β	$N_{\rm bulge}$	α	TS	$N_{\rm disk}$	z_0[kpc]	β	$N_{\rm bulge}$	α	TS
1	25600^{+5900}_{-5200}	$0.72^{+0.22}_{-0.22}$	$1.37^{+0.13}_{-0.13}$	0	$\cdots$	0	24500^{+5700}_{-5000}	$0.76^{+0.23}_{-0.23}$	$1.33^{+0.14}_{-0.14}$	0	$\cdots$	0
2	4670^{+1350}_{-1230}	$0.69^{+0.21}_{-0.21}$	$1.25^{+0.12}_{-0.12}$	1380^{+370}_{-310}	2.60	53	3710^{+1270}_{-1150}	$0.75^{+0.23}_{-0.23}$	$1.26^{+0.12}_{-0.12}$	1310^{+350}_{-290}	2.60	54
3	4360^{+1370}_{-1180}	$0.68^{+0.20}_{-0.20}$	$1.24^{+0.11}_{-0.11}$	1430^{+380}_{-320}	$2.57^{+0.27}_{-0.27}$	58	3660^{+1210}_{-1110}	$0.73^{+0.22}_{-0.22}$	$1.25^{+0.12}_{-0.12}$	1350^{+330}_{-300}	$2.65^{+0.28}_{-0.28}$	59

Table 2
Results from the maximum likelihood fits to the number of observed PSR candidates.

Note. — Best fit and 1σ uncertainty for $N_{\rm disk}$, z_0, β, $N_{\rm bulge}$ and α and TS with respect to the null hypothesis (first row) for the Alt. (left block) and Off. IEM (right block) and first (top block with pixel size 3.3°) and second (bottom with pixel size 6.0°) setup of spatial and energy flux bins (see the text for further details on the binning).

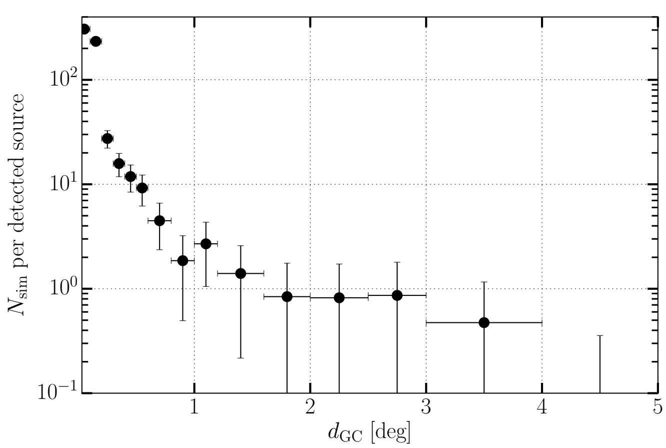

Figure 8. Average number of simulated sources ($N_{\rm sim}$) within the 95% positional error of each detected simulated PSR candidate as a function of angular distance from the GC ($d_{\rm GC}$).

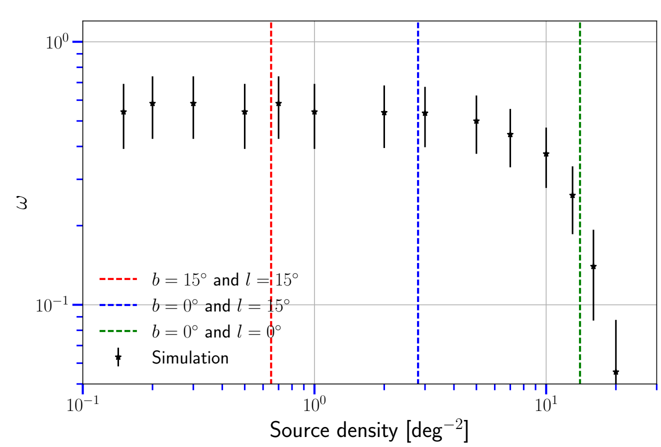

Figure 9. Efficiency ω for the detection of PSR-like sources as a function of the density of simulated sources. We also display with vertical lines the density of sources at three different locations in the inner part of the Galaxy considering the model for disk and bulge PSRs explained in Secs. 5 to 6.2.

cm^{-2} s^{-1}).

Specifically, we expect the number of bright pulsars predicted by the model, $N^{\rm model}_{S>S_0}(\lambda)$ to lie between the number of identified PSRs (111) and the number of sources with curved SEDs in the 3FGL (237); see Figure 4. We have implemented this constraint using a Gaussian prior:

$$\mathcal{L}_{\rm prior} = \frac{(N^{\rm model}_{S>S_0}(\lambda) - N^{\rm data}_{S>S_0})^2}{2\sigma_N{}^2}, \quad (5)$$

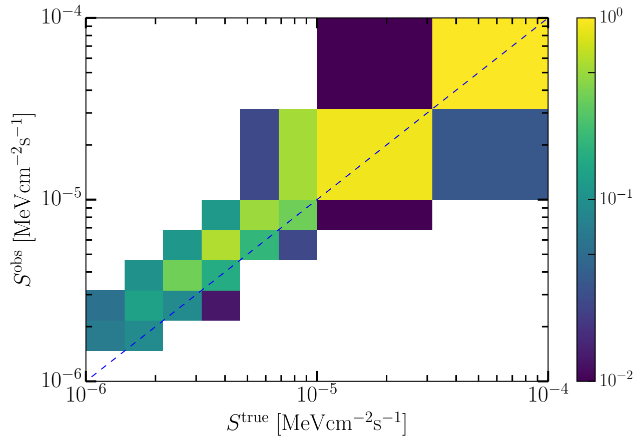

Figure 10. Corrected efficiency (Ω) for energy fluxes between 10^{-6} and 10^{-4} MeV cm^{-2}s^{-1}. The color scale shows the fraction of sources generated with $S^{\rm true}$ detected with $S^{\rm obs}$.

where we take $N^{\rm data}_{S>S_0} = 174$ and $\sigma_N = 63$ from the middle and half-width of the range 111 to 237.

In Table 2 we report the results of the maximum likelihood analysis when different scenarios are considered. We list the results derived with the Off. (left block) and Alt. IEM (right block) and for different spatial binning. Case A (top block) is for a bin size 3.3° while case B (bottom block) is for bin size 6.0°.

We use 3.3° bins since the brighter part of the excess (around 90% of its total flux) is within 10° of the GC. With 3.3° binning, the GC excess is well resolved. We use six equally spaced logarithmic bins in energy flux between 10^{-6} MeV cm^{-2} s^{-1} and 10^{-5} MeV cm^{-2} s^{-1} and two additional bins between $[1, 10] \cdot 10^{-5}$ MeV cm^{-2} s^{-1} since for the brightest fluxes the efficiency is flat and very nearly equal to 1 (see Figure 7).

We define as our null hypothesis H_0 that the observed distribution of PSR candidates comes from the PSR disk population with $N_{\rm disk}$, z_0 and β as the free parameters. Results for the null hypothesis are given in the first row in Table 2. In this model $N_{\rm disk}$ is found to be in the range $[23000, 26000]$, $z_0 = [0.63, 0.76]$ and $\beta = [1.33, 1.37]$ depending on the IEM and pixel size. This gives a number of PSRs, $N^{\rm model}_{S>S_0}$, that is around 350 and is only marginally consistent with the range we have estimated from the 3FGL (see Figure 4).

The fitted index of the luminosity function, $\beta = 1.34 \pm 0.07$ for the null hypothesis (for Off. IEM and 3.3° pixel size) is softer than the index of the distribution of detected PSRs ($\beta = 1.20 \pm 0.08$, see Figure 3). We attribute the difference to contamination from the fainter Galactic bulge PSR population in the 40° × 40° ROI.

To test the possibility that we have over-constrained the spatial morphology of the Galactic disk PSR population we also freed n and σ, the two parameters of the Lorimer profile. The likelihood improves significantly with respect to H_0 with $TS \sim 40$ but the best-fit values for these two parameters are $n \approx 0$ and $\sigma \approx 1.2$ kpc. The initial n, σ values for the Lorimer profile give $\rho = 0$ at the GC, increasing to a maximum around 3 kpc, and decreasing at larger distances. With the inferred best-fit values the disk population has a peak at $r = 0$ kpc, becoming thus a sort of bulge very similar to the Galactic bulge PSR distribution. Therefore, with this spatial freedom for the model of the disk population the results suggest the existence of a population of PSRs in the inner part of the Galaxy.

Adding a Galactic bulge PSR population with the number of sources of this component $N_{\rm bulge}$ free to vary we find a large improvement in the maximum likelihood with $TS = [53, 63]$ for Alt./Off. IEM. This TS is associated with the addition of only one free parameter, namely $N_{\rm bulge}$. Thus $TS = [53, 63]$ formally corresponds to a significance at the level of 7.3 to 7.9 standard deviations. In this case the best fit for the number of PSRs in the two populations is $N_{\rm bulge} = [1310, 1580]$ and $N_{\rm disk} = [3500, 4700]$. Finally, β is $[1.23, 1.26]$.

If we free the parameter α, the slope of the radial distribution of Galactic bulge PSRs, the maximum likelihood is slightly greater than before ($TS = [58, 69]$) with $\alpha = [2.55, 2.65]$, which is consistent with a generalized NFW distribution as found for the GC excess by Calore et al. (2015b); Daylan et al. (2016) and Ajello et al. (2016). In this case we have two additional degrees of freedom with respect to H_0, $(N_{\rm bulge}, \alpha)$, so $TS = [58, 69]$ corresponds to a significance at the level of 7.3 to 8.0 standard deviations.

Our maximum likelihood analysis of the spatial distribution and energy flux of PSR candidates supports the existence of a disk PSR population with $\beta \sim 1.25$, $z_0 \sim 0.70$ kpc, distributed with a Lorimer spatial profile (Lorimer 2004) with $N_{\rm disk} \sim 3500$ PSRs and a Galactic bulge PSR population with around $N_{\rm bulge} \sim 1300$ PSRs distributed with $\rho \propto r^{-2.6}$ with respect to the GC. This result is consistent with the number of known PSRs and unassociated spectrally curved sources in the 3FGL. Moreover the Galactic bulge population is consistent with the properties of the GC excess. In the left panel of Figure 11 we show the latitude profile of the γ-ray intensity from Galactic bulge PSRs compared to GC excess from Calore et al. (2015b) and Ajello et al. (2016). Moreover, the total energy spectrum of this PSR population is compatible with the spectrum of the excess (see right panel of Figure 11). The values of $N_{\rm disk}$ and $N_{\rm bulge}$ are somewhat arbitrary as they depend strongly on both the integration ranges used to define them and the index of the PSR luminosity function. However, since we have used the same integration range and luminosity function for both populations, these definitions drop out of the ratio $N_{\rm disk}/N_{\rm bulge}$. Accordingly, we prefer to state this key result as $N_{\rm disk}/N_{\rm bulge} \sim 2.7$.

9. TESTING THE DARK MATTER SCENARIO

A widely studied alternative interpretation for the GC excess is that it is produced by DM particle annihilations in the DM halo of our Galaxy. This DM halo would be densest in the inner part of the Galaxy, which would correspondingly have the most intense γ-ray emission. The GC excess can be interpreted as being consistent with annihilation through the $b\bar{b}$ channel of a DM particle with a mass around 50 GeV and cross section near the canonical thermal relic value (e.g., Calore et al. 2015a).

We test this DM annihilation hypothesis by considering the spatial distribution of the excess from Ajello et al. (2016) and making one simulation of the γ-ray emission in our ROI including the IEM, isotropic template, a disk population of 2800 PSRs, 900 blazars and the DM GC excess template. With respect to the previous simulation we thus replace the Galactic bulge PSR population with the DM template. We then analyze the simulation using as a starting point only the Off. IEM and the isotropic template. We extract 96 PSR candidates from the PSR disk population and 34 spurious PSR candidates from the DM excess template. All the spurious PSR

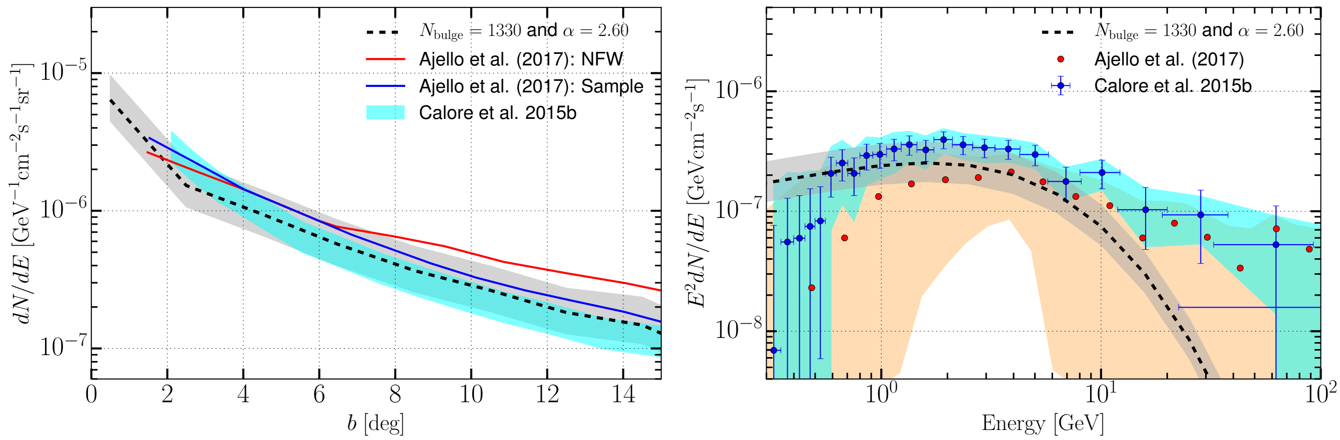

Figure 11. Same as Figure 5 except for the best-fit scenario of Table 2 for the Off. IEM and 3.3° pixel size instead of the baseline model used for simulations.

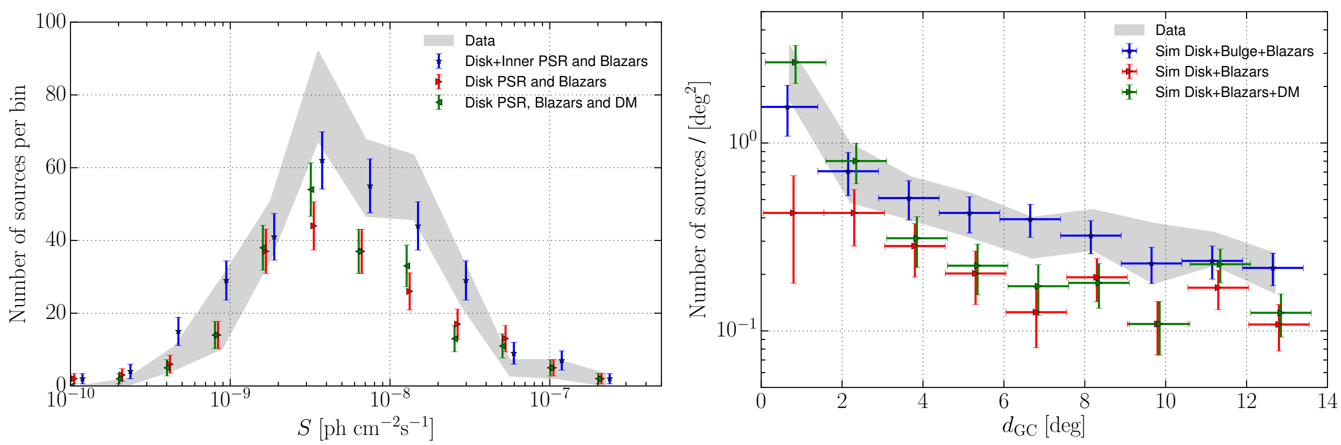

Figure 12. Flux histogram (left panel) and angular distance distribution (right panel) of sources detected with $TS > 25$ in the analysis of the real sky with both the IEMs (gray band) and with simulations that include blazars/disk PSRs (red data) or blazars/disk/Galactic bulge PSRs (blue data) or blazars/disk/ and DM contribution (green data).

candidates are located within a few degrees of the GC. This is not consistent with the observed distribution of PSR candidates. In Figure 12 we show the flux histogram and distribution of angular distance from the GC of sources detected with $TS > 25$, both for the analysis of the real sky and of simulations of several different scenarios. Only the scenario with both the disk and Galactic bulge PSRs is consistent with the observed distribution of sources. The scenario with only blazars and a disk population of PSRs under-predicts the number of PSR candidates for all angular distances from the GC. Adding DM emission resolves this discrepancy only within a few degrees of the GC. Similarly, the energy flux distribution would have a deficit of sources detected with a photon flux $\sim \mathcal{O}(10^{-8} \mathrm{ph\,cm}^{-2}\mathrm{s}^{-1})$ if we did not consider the Galactic bulge population of PSRs.

10. CONCLUSIONS

We have analyzed 7.5 years of Pass 8 *Fermi*-LAT data for the energy range $[0.3, 500]$ GeV in a $40^\circ \times 40^\circ$ around the GC in order to provide a list of PSR candidates and test the pulsar interpretation of the GC excess. Employing two IEMs we detect about 400 sources, a factor of about two more than in the 3FGL catalog (Acero et al. 2015) and five more than in the 1FIG (Ajello et al. 2016) (derived for $[1, 100]$ GeV and for $15^\circ \times 15^\circ$); these latter analyses were based on shorter time intervals of data than we consider here. We then studied the SEDs of γ-ray PSRs and 3FGL blazars using a PLE shape and found that the distributions of photon index and energy cutoff parameters for these two populations are very well separated, with typical values of $\Gamma < 2$ and $E_{\rm cut} < 10$ GeV for PSRs. Moreover, about 82% of PSRs and only 9% of blazars have $TS_{\rm curv}^{\rm PLE} > 9$. We thus use the selection criteria $TS_{\rm curv}^{\rm PLE} > 9$, $\Gamma < 2$ and $E_{\rm cut} < 10$ GeV to extract PSR candidates from our seed list, finding 66 sources detected with both IEMs.

We took the distribution of spectral parameters from the 210 identified γ-ray PSRs and the luminosity distribution of PSRs within 3 kpc [8]. We used parameters given by Lorimer (2004); Calore et al. (2014) to model the spatial distribution of the disk population of PSRs. With this model, we find that given the number and distributions of unassociated 3FGL sources with curved SED we constrain the number of Galactic disk PSRs to be in the range $[1400, 5600]$ for a luminosity function with slope 1.20 and $L_\gamma = [10^{31}, 10^{36}]$ erg s^{-1}. Similarly, we used the latitude profile and energy spectrum of the GC excess (e.g., Calore et al. 2015b; Ajello et al. 2016) to model the Galactic bulge PSR population and found that it must include 500–2300 sources (most of them unresolved) if it is to explain the GeV excess.

We used a maximum likelihood analysis to characterize the disk and bulge populations of PSRs. We compared the observed distribution of PSR candidates with the models of Galactic disk and Galactic bulge PSR populations.

If we consider only the disk population, the fitted number of sources is $N_{\rm disk} \approx 23000$ with a slope of the luminosity function of ~ 1.35 (for $L_\gamma = [10^{31}, 10^{36}]$ erg s^{-1}). This result is marginally consistent with the upper limit inferred from γ-ray PSRs and 3FGL sources with curved SEDs.

Moreover, freeing the spatial distribution parameters of the Galactic disk PSR population effectively made the disk bulge-like. Adding a bulge population of PSRs improves the overall maximum likelihood at the level of more than 7 standard deviations.

The best-fit values for the number of PSRs in the disk and the bulge are $N_{\rm disk} \sim 3500$ and $N_{\rm bulge} \sim 1300$ with a slope of the luminosity function of ~ 1.25 (for $L_\gamma = [10^{31}, 10^{36}]$ erg s^{-1}). We thus find that the best-fit model requires 2.7 PSRs in the disk for each PSR in the Galactic bulge population. These values are consistent with γ-ray PSRs in the 3FGL and with the spatial distribution and energy spectrum of the GC excess.

The number of disk PSRs that we find with our analysis is a small fraction of the estimated 30,000 detectable radio pulsars (Levin et al. 2013; Grégoire & Knödlseder 2013; Lorimer 2013) or of the independent estimate of 20000 young pulsars beaming toward Earth (Johnston & Karastergiou 2017). Judging the consistency of these two estimates of the underlying pulsar population requires detailed analysis of the correlation between radio and γ-ray fluxes and of the relative effects of beaming, and is beyond the scope of this paper.

We demonstrated also that a Galactic DM halo would produce only a small fraction of the detected PSR candidates, and those candidates would typically be much closer to the GC than the observed candidates.

In summary, we confirm the findings of Lee et al. (2015); Bartels et al. (2016) of a population of point sources in the Galactic bulge that can explain the GeV excess. Additionally, we present conclusive evidence that this population consists of sources with PSR-like spectra and whose luminosity function matches that of known γ-ray PSRs. Definitive confirmation that these sources are in fact pulsars will require detection of pulsations for several of the sources. Furthermore, the measurement of the pulsation periods of these sources would immediately give significant insight into the origins of the population.

Facilities: Fermi.

The *Fermi* LAT Collaboration acknowledges generous ongoing support from a number of agencies and institutes that have supported both the development and the operation of the LAT as well as scientific data analysis. These include the National Aeronautics and Space Administration and the Department of Energy in the United States; the Commissariat à l'Energie Atomique and the Centre National de la Recherche Scientifique/Institut National de Physique Nucléaire et de Physique des Particules in France; the Agenzia Spaziale Italiana and the Istituto Nazionale di Fisica Nucleare in Italy; the Ministry of Education, Culture, Sports, Science and Technology (MEXT), High Energy Accelerator Research Organization (KEK), and Japan Aerospace Exploration Agency (JAXA) in Japan; and the K. A. Wallenberg Foundation, the Swedish Research Council, and the Swedish National Space Board in Sweden. Additional support for science analysis during the operations phase is gratefully acknowledged from the Istituto Nazionale di Astrofisica in Italy and the Centre National d'Etudes Spatiales in France.

MDM and EC acknowledge support by the NASA Fermi Guest Investigator Program 2014 through the Fermi multi-year Large Program N. 81303 (P.I. E. Charles).

REFERENCES

Abazajian, K. N. 2011, JCAP, 3, 010
Abazajian, K. N., Canac, N., Horiuchi, S., & Kaplinghat, M. 2014, Phy. Rev. D, 90, 023526
Abazajian, K. N. & Kaplinghat, M. 2012, Phy. Rev. D, 86, 083511
Abdo, A. A., Ackermann, M., Ajello, M., et al. 2010a, ApJS, 188, 405
Abdo, A. A., Ackermann, M., Ajello, M., et al. 2010b, ApJ, 720, 435
Abdo, A. A., Ajello, M., Allafort, A., et al. 2013, ApJS, 208, 17
Acero, F., Ackermann, M., Ajello, M., et al. 2015, ApJS, 218, 23
Acero, F., Ackermann, M., Ajello, M., et al. 2016, ApJS, 223, 26
Ackermann, M., Ajello, M., Albert, A., et al. 2015, ApJ, 799, 86
Ackermann, M., Albert, A., Atwood, W. B., et al. 2014, ApJ, 793, 64
Ackermann, M. et al. 2017, Accepted in ApJ
Ajello, M., Albert, A., Atwood, W. B., et al. 2016, ApJ, 819, 44
Albert, A., Anderson, B., Bechtol, K., et al. 2017, ApJ, 834, 110
Atwood, W., Albert, A., Baldini, L., et al. 2013, ArXiv:1303.3514
Bartels, R., Krishnamurthy, S., & Weniger, C. 2016, Phys. Rev. Lett., 116, 051102
Brandt, T. D. & Kocsis, B. 2015, ApJ, 812, 15
Calore, F., Cholis, I., McCabe, C., & Weniger, C. 2015a, Phy. Rev. D, D91, 063003
Calore, F., Cholis, I., & Weniger, C. 2015b, JCAP, 1503, 038
Calore, F., Di Mauro, M., Donato, F., & Donato, F. 2014, ApJ, 796, 1
Calore, F., Di Mauro, M., Donato, F., Hessels, J. W. T., & Weniger, C. 2016, ApJ, 827, 143
Carlson, E., Linden, T., & Profumo, S. 2016, Phys. Rev. Lett., 117, 111101
Carlson, E. & Profumo, S. 2014, Phy. Rev. D, 90, 023015
Cholis, I., Evoli, C., Calore, F., et al. 2015a, JCAP, 1512, 005
Cholis, I., Hooper, D., & Linden, T. 2014, ArXiv:1407.5583
Cholis, I., Hooper, D., & Linden, T. 2015b, JCAP, 1506, 043
Daylan, T., Finkbeiner, D. P., Hooper, D., et al. 2016, Physics of the Dark Universe, 12, 1
Di Mauro, M. & Donato, F. 2015, Phy. Rev. D, 91, 123001
Dormody, M., Johnson, R. P., Atwood, W. B., et al. 2011, ApJ, 742, 126
Gaggero, D., Taoso, M., Urbano, A., Valli, M., & Ullio, P. 2015, JCAP, 1512, 056
Goodenough, L. & Hooper, D. 2009, ArXiv:0910.2998
Gordon, C. & Macías, O. 2013, Phy. Rev. D, 88, 083521
Grégoire, T. & Knödlseder, J. 2013, Astron. Astrophys., 554, A62
Guillemot, L., Smith, D. A., Laffon, H., et al. 2016, A&A, 587, A109
Hooper, D. & Goodenough, L. 2011, Phys. Lett., B697, 412
Hooper, D. & Mohlabeng, G. 2016, ApJ, 1603, 049
Hooper, D. & Slatyer, T. R. 2013, Physics of the Dark Universe, 2, 118
Johnston, S. & Karastergiou, A. 2017, ArXiv:1702.03616
Keith, M. J., Jameson, A., van Straten, W., et al. 2010, MNRAS, 409, 619
Kramer, M. & Stappers, B. 2015, Advancing Astrophysics with the Square Kilometre Array (AASKA14), 36
Kravtsov, A. V., Klypin, A. A., Bullock, J. S., & Primack, J. R. 1998, ApJ, 502, 48
Kruskal, J. B. 1956, Proceedings of the American Mathematical Society, 7, 48
Lee, S. K., Lisanti, M., & Safdi, B. R. 2015, JCAP, 1505, 056
Levin, L., Bailes, M., Barsdell, B. R., et al. 2013, MNRAS, 434, 1387
Lorimer, D. R. 2004, in IAU Symposium, Vol. 218, Young Neutron Stars and Their Environments, ed. F. Camilo & B. M. Gaensler, 105
Lorimer, D. R. 2013, in IAU Symposium, Vol. 291, Neutron Stars and Pulsars: Challenges and Opportunities after 80 years, ed. J. van Leeuwen, 237–242
Manchester, R. N., Hobbs, G. B., Teoh, A., & Hobbs, M. 2005, AJ, 129, 1993
Mattox, J. R., Bertsch, D. L., Chiang, J., et al. 1996, ApJ, 461, 396
Mirabal, N. 2013, MNRAS, 436, 2461
Navarro, J. F., Frenk, C. S., & White, S. D. M. 1996, ApJ, 462, 563
Petrović, J., Serpico, P. D., & Zaharijaš, G. 2014, JCAP, 1410, 052
Petrović, J., Serpico, P. D., & Zaharijas, G. 2015, JCAP, 1502, 023
Steigman, G., Dasgupta, B., & Beacom, J. F. 2012, Phy. Rev. D, 86, 023506
Stovall, K., Lorimer, D. R., & Lynch, R. S. 2013, Classical and Quantum Gravity, 30, 224003
Strong, A. W. 2007, Astrophys. Space Sci., 309, 35
Su, M., Slatyer, T. R., & Finkbeiner, D. P. 2010, ApJ, 724, 1044

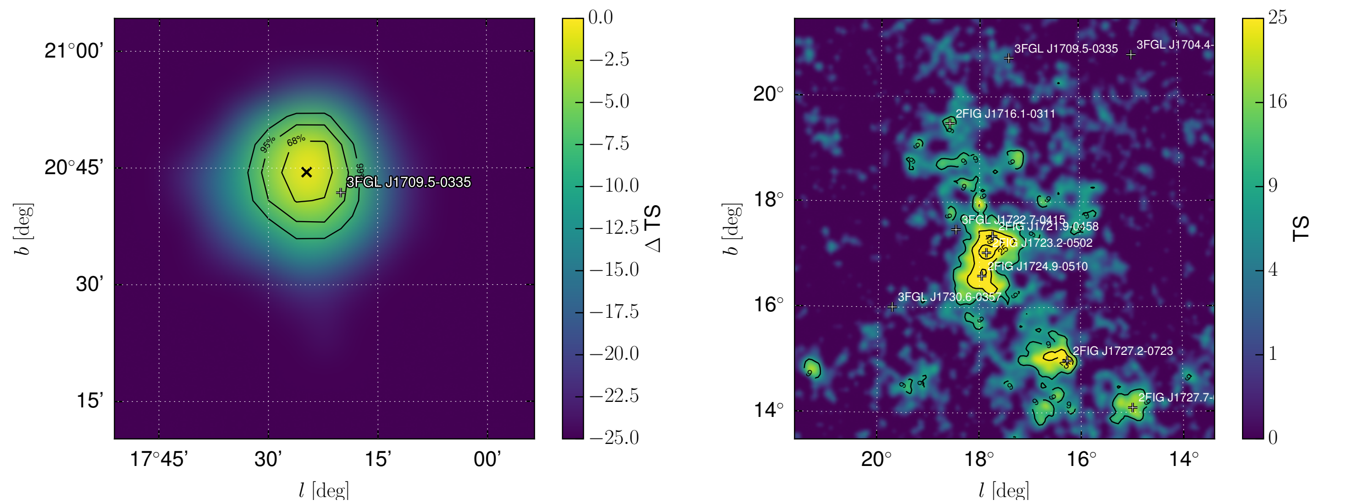

Figure 13. Left panel: Positional uncertainty contours and best-fit position (solid black lines and x marker) from the localization of 3FGL J1709.5−0335. The color scale shows the difference in TS with respect to the best-fit position of the source. The cross is the position of this source in 3FGL. Right panel: TS map of the ROI evaluated with a test source with a point-source morphology and a PL spectrum with photon index of 2. The background model includes the IEM, isotropic template, and 3FGL sources with $TS > 49$.

Winter, M., Zaharijas, G., Bechtol, K., & Vandenbroucke, J. 2016, ApJ, 832, L6

Yuan, Q. & Zhang, B. 2014, Journal of High Energy Astrophysics, 3, 1

APPENDIX

A. ANALYSIS PIPELINE AND DESCRIPTION OF FERMIPY TOOLS

We analyze each ROI with a pipeline based on the `Fermipy` package and the *Fermi* Science Tools. In the following description, we denote with italics the `Fermipy` methods and configuration parameters used in each step of the pipeline.

We start the analysis of each region with a model that includes 3FGL sources with TS > 49, the IEM, and the isotropic template and begin by optimizing the spatial and spectral parameters of this model. We first perform a global fit of the spectral parameters for all components in the model. For the global fit we retain the spectral model (PL, LP or PLE) reported by the 3FGL. We then relocalize all 3FGL point sources using the *localize* method. This method generates a map of the model likelihood versus source position in the vicinity of the nominal 3FGL position and finds the best-fit position and errors by fitting a 2D parabola to the log-likelihood values in the vicinity of the peak. When localizing a source, we free the normalization of the IEM and isotropic template and spectral parameters of sources within 3° of the source of interest. After relocalizing 3FGL sources, we repeat the global fit of the spectral parameters of all components.

On average, 3FGL sources move by $0.04°$ in the relocalization step. This is of the same order as the 68% location uncertainty radius for most 3FGL sources (Acero et al. 2015). As an example, in the left panel of Figure 13 we show the result of the relocalization for 3FGL J1709.5−0335. The new position is offset by $0.087°$ with respect to the 3FGL position and the 3FGL 68% positional uncertainty is $0.064°$.

After relocalizing the 3FGL sources, we add new source candidates to the model using the *find_sources* method. This method iteratively refines the model by identifying peaks in a TS map of the region with $\sqrt{TS} >$ *sqrt_ts_threshold* and adding a new source at the position of each peak. After each iteration a new TS map is generated with an updated background model that incorporates sources found in the previous iteration. This procedure is repeated until no peaks are found with amplitude larger than *sqrt_ts_threshold*. To minimize the likelihood of finding multiple peaks associated with a single source, the algorithm restricts the separation between peaks found in an iteration to be greater than *min_separation* by excluding peaks that are within this distance of a peak with higher TS.

We run *find_sources* with a point-source test source model with a PL spectrum and a fixed photon index of $\Gamma = 2$. We use *sqrt_ts_threshold* $= 4$ and *min_separation*$= 0.4°$. The result is a list of source candidates with $TS > 16$. On average we detected about six sources with $TS > 25$ per ROI.

In the right-hand panel of Figure 13 we display an example TS map derived prior to the source-finding step when only the IEM, isotropic template and 3FGL sources with $TS > 49$ are included. From this figure we note that a region with $TS > 25$ is located in the center of the ROI, near $(l, b) = (17.5°, 17°)$ from which our analysis extracted three new sources with $TS > 25$.

We derive the SED for each source candidate in our list using the *sed* method. A likelihood analysis is performed in each energy bin independently, using for the spectrum of the source a PL shape with a fixed photon index of 2 and normalization free to vary. In this procedure we also leave free the normalizations of the IEM, isotropic template, and the normalizations of sources within 3° of the source of interest. As an example, in Figure 14 the SED of 3FGL J1730.6−0357 is reported together with a fit of a PLE spectrum. 3FGL J1730.6−0357 has $TS_{\rm curv}^{\rm PLE} = 40$ meaning that it has a significant curvature. The fit with a PLE in fact gives a spectral index of 0.5 and energy cutoff of 1.4 GeV.

To avoid finding duplicate sources in regions where our ROIs overlap, we remove sources that are found in more than one ROI and that have an angular separation smaller than $0.2°$. Specifically we keep the version of the source that is closest to the center of the ROI in which it was found.

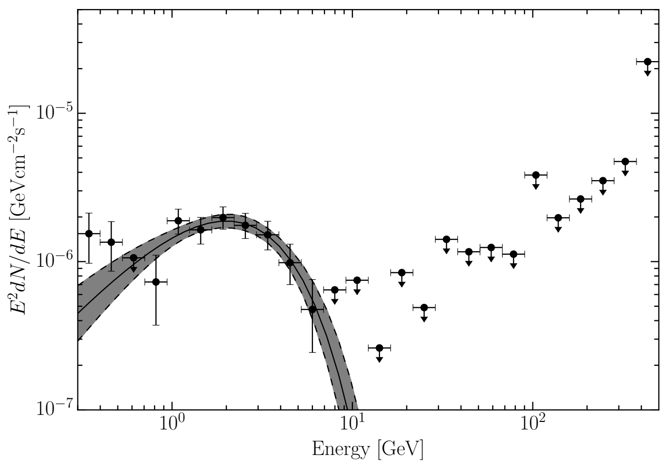

Figure 14. SED of 3FGL J1730.6−0357 (black points) and best-fit PLE parameterization with 1σ uncertainty band (black line and gray band).

B. MINIMUM SPANNING TREE SOURCE CLUSTER-FINDING

To avoid placing spurious point sources in regions where the IEM under-predicted the Galactic diffuse emission we applied a source clustering algorithm based on the minimum spanning tree (MST) algorithm. The MST algorithm calculates how to connect points with minimum total length of the connections (Kruskal 1956). The *fermipy.cluster_sources* module applies the MST algorithm to identify clusters of sources by joining sets of sources within a maximum connection distance (the $dist$ parameter) and retaining those clusters with at least a specified minimum number of sources (the $nsrc$ parameter). We tested different values for $dist$ and $nsrc$. We found that using $nsrc \geq 4$ generally avoided creating spurious clusters around chance spatial coincidences. For $nsrc = 4$, we found that using $dist = 0.6°$ selected a few clusters that were spatially associated with known regions of complicated Galactic diffuse emission, such as supernova remnants and the GC. Using larger values, such as $dist = 1.0°$, resulted in clusters consisting of chains of sources up to $\sim 4°$ long in the Galactic plane. Using $dist \leq 0.3°$ and $nsrc = 4$, resulted in no clusters being found with either IEM. The same four clusters found using the Off. IEM and the values $dist = 0.6°$ and $nsrc = 4$ were also found using $dist = 0.7°$, and only the cluster near the GC was found using $dist = 0.5°$. In light of these studies, we adopted the value $dist = 0.6°$ and $nsrc = 4$ and obtain the results presented in Section 3.

C. SOURCE LIST AND CONTENTS OF FITS FILE

Together with this paper, we are releasing the list of sources detected in our analysis as a `FITS` file. The file contains a single binary table with the source data. The list includes 469 sources detected with $TS > 25$ in a region with $|b| < 20°$ and $|l| < 20°$. The table has one row per source; the column names and contents are described in Table 3. When applicable the units of the columns are given by the header keywords following the `FITS` standard. All of the spectral parameters are taken from the ROI optimization procedure described in Appendix A.

D. GENERATING SIMULATED DATA WITH FERMIPY

We use the *simulate_roi* method to simulate the binned γ-ray counts data in each ROI using the maximum-likelihood model of the ROI. Specifically, the method generates “model cubes” of the expected number of γ-ray counts in each pixel and energy bin in the ROI for the time interval of our analysis. The method then generates Poisson-distributed random numbers with expectation values drawn from the model cube for each pixel and energy bin and produces a simulated binned counts maps for each ROI. This procedure results in simulated γ-ray counts maps that are statistically identical to those produced with *gtobssim*, which simulates individual γ rays and convolves them with the instrument response model. The *simulate_roi* method is many times faster than *gtobssim*, making the extensive simulations we have performed much more tractable.

E. TESTING PSR SELECTION CRITERIA WITH SIMULATED DATA

As discussed in Section 4, ∼90% of blazars in the 3FGL catalog have an SED modeled with PL shape while the remaining 10% are modeled with a LP. On the other hand, about 82% of PSRs have energy spectra consistent with a PLE. Employing the parameter $TS_{\rm curv}^{\rm PLE}$ and making spectral fits of blazars and PSRs with a PLE model we have shown that the criteria $TS_{\rm curv}^{\rm PLE} > 9$, $\Gamma < 2.0$ and $E_{\rm cut} < 10$ GeV work very well to separate the PSR and blazar populations.

In this Appendix we investigate how these criteria work for a simulated test population of sources with curved spectra compatible with a PLE, but with a slightly larger energy cutoff and softer photon index with respect to PSRs. We want to test if this additional population would severely contaminate our PSR candidates. For this we simulate a bulge population of PSRs as explained in Section 6.2 and 1500 sources with a photon index of 2.3 ± 0.2 and energy cutoff of $\log_{10}(E_{\rm cut}[{\rm MeV}]) = 4.48 \pm 0.25$ uniformly distributed in the GC region. We choose these distributions for the energy spectrum parameters to demonstrate that a putative population of sources with a curved SED and with a distribution of Γ and $E_{\rm cut}$ that is fairly well separated from the PSR-like criteria is not going to contaminate significantly our selection of PSR-like sources because of mis-estimation of the spectral parameters.

Contents	Column Name	Units	Uncertainty
Source designation	`Source_Name`	···	···
Right ascension	`RAJ2000`	[deg]	···
Declination	`DEJ2000`	[deg]	···
Galactic longitude	`GLON`	[deg]	···
Galactic latitude	`GLAT`	[deg]	···
Containment radius (68%)	`pos_68`	[deg]	···
Containment radius (95%)	`pos_95`	[deg]	···
TS	TS	···	···
$TS_{\rm curv}^{\rm PLE}$	`TS_curv`	···	···
Integrated photon flux between $E = [0.3, 500]$ GeV	`Flux300`	[ph cm^{-2} s^{-1}]	`Unc_F300`
Integrated energy flux between $E = [0.3, 500]$ GeV	`Energy_Flux300`	[MeV cm^{-2} s^{-1}]	`Unc_Energy_Flux300`
Functional form of the SED	`SpectrumType`	···	···
Spectral index	`Spectral_Index`	···	`Unc_Spectral_Index`
Cutoff energy (for PLE)	`Cutoff`	[MeV]	`Unc_Cutoff`
Curvature parameter, β (for LP)	`beta`	···	`Unc_beta`
IEM with which the source is detected	`IEM`	···	···
Associated 3FGL source	`3FGL_Name`	···	···
Classification of 3FGL source	`3FGL_Class`	···	···
Cluster membership (Off. IEM)	`Cluster_Off`	···	···
Cluster membership (Alt. IEM)	`Cluster_Alt`	···	···

Table 3
Contents of the 2FIG source list `FITS` table.

Note. — When a source is detected with both of the IEM models the reported position, SED parameters as well as the photon and energy fluxes are the ones found with the Off. IEM. We report the TS for curvature, and the SED parameters for the PLE only for PSR-like sources as defined in the main text. For sources with a 3FGL association that was modeled with a LP spectrum we also report the curvature parameter, β. The `IEM` column has value "Off", "Alt" or "Off/Alt". The `Cluster_Off` and `Cluster_Alt` columns give the index of the cluster to which a given source is associated, if any.

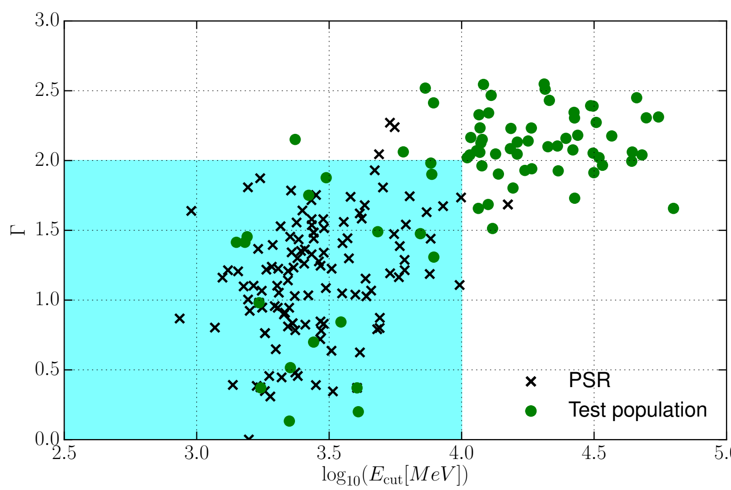

Figure 15. Photon index Γ and energy cutoff $E_{\rm cut}$[MeV] of PSRs (black points) and for a simulated test population of sources isotropically distributed in the sky (red points). See the text for further details on the SED of these sources.

We simulate fluxes of sources for this population from the source count distribution of blazars derived by Abdo et al. (2010b). We use the same analysis as used for the derivation of the source list in the real sky. For the SED we consider a PLE shape and evaluate the best-fit parameters for Γ and $\log_{10}(E_{\rm cut})$. Then we select the sources detected with $TS > 25$ and $TS_{\rm curv}^{\rm PLE} > 9$. The result for the values of Γ and $\log_{10}(E_{\rm cut})$ is displayed in Figure 15. Also the detected sources satisfying $TS_{\rm curv}^{\rm PLE} > 9$ maintain a very good separation in the $\Gamma - \log_{10}(E_{\rm cut})$ plane. Only 6% of the non-PSR sources detected with $TS > 25$ have measured $\Gamma < 2.0$ and $E_{\rm cut} < 10$ GeV and $TS_{\rm curv}^{\rm PLE} > 9$. This result means that the presence of a putative source population with an SED modeled with a PLE but with a softer photon index and higher-energy cutoff would produce a contamination that is small with respect to our PSR candidates.